



# Improved ELMv1-ECA Simulations of Zero-Curtain Periods and Cold-season CH<sub>4</sub> and CO<sub>2</sub> Emissions at Alaskan Arctic Tundra Sites

Jing Tao<sup>1,2</sup>, Qing Zhu<sup>1</sup>, William J. Riley<sup>1</sup>, Rebecca B. Neumann<sup>2</sup>

<sup>1</sup>Climate and Ecosystem Sciences Division, Lawrence Berkeley National Laboratory, Berkeley, CA, 94720, USA

5 <sup>2</sup>Department of Civil and Environmental Engineering, University of Washington, Seattle, WA, 98195, USA

*Correspondence to:* Jing Tao (JingTao@lbl.gov)

**Abstract.** Field measurements have shown that cold-season methane (CH<sub>4</sub>) and carbon dioxide (CO<sub>2</sub>) emissions contribute a substantial portion to the annual net carbon emissions in permafrost regions. However, most earth system land models do not accurately reproduce cold-season CH<sub>4</sub> and CO<sub>2</sub> emissions, especially over the shoulder (i.e., thawing and freezing) seasons.

10 Here we use the Energy Exascale Earth System Model (E3SM) land model version 1 (ELMv1-ECA) to tackle this challenge and fill the knowledge gap of how cold-season CH<sub>4</sub> and CO<sub>2</sub> emissions contribute to the annual totals at Alaska Arctic tundra sites. Specifically, we improved the ELMv1-ECA soil water phase-change scheme, environmental controls on microbial activity, and cold-season methane transport module. Results demonstrate that both soil temperature and the duration of zero-curtain periods (i.e., the fall period when soil temperatures linger around 0°C) simulated by the updated  
15 ELMv1-ECA were greatly improved, e.g., the Mean Absolute Error in zero-curtain durations at 12 cm depth was reduced by 62% on average. Furthermore, the simulated cold-season emissions at three tundra sites were improved by 84% and 81% on average for CH<sub>4</sub> and CO<sub>2</sub>, respectively. Overall, CH<sub>4</sub> and CO<sub>2</sub> emitted during the early cold season (Sep. and Oct.), which often includes most of the zero-curtain period in Arctic tundra, accounted for more than 50% of the total emissions throughout the entire cold season (Sep. to May). From 1950 to 2017, both CO<sub>2</sub> emissions during the 12 cm depth zero-  
20 curtain period and during the entire cold season showed increasing trends, for example, of 0.26 gC m<sup>-2</sup> year<sup>-1</sup> and 0.38 gC m<sup>-2</sup> year<sup>-1</sup> at Atkasuk. This study highlights the importance of zero-curtain periods in facilitating CH<sub>4</sub> and CO<sub>2</sub> emissions from tundra ecosystems.



## 1 Introduction

25 Cold-season carbon emissions from the Arctic tundra could potentially offset warm-season net carbon uptake under 21<sup>st</sup>  
 century warming climate (Commane et al., 2017; Oechel et al., 2014; Oechel et al., 2000; Koven et al., 2011; Piao et al.,  
 2008; Natali et al., 2019; Belshe et al., 2013; Fahnestock et al., 1998; Jones et al., 1999). Field measurements have indicated  
 large cold-season CO<sub>2</sub> losses over Arctic tundra ecosystems (Oechel et al., 2014; Natali et al., 2019). Also, CH<sub>4</sub> emitted from  
 30 September to May were found to contribute more than 50% of the annual total CH<sub>4</sub> emissions from Alaska upland tundra  
 sites (Zona et al., 2016; Taylor et al., 2018). Despite the importance of cold-season carbon emissions and their sensitivity to  
 changing climate, prevailing earth system land models do not accurately reproduce cold-season CH<sub>4</sub> and CO<sub>2</sub> emissions and  
 their contributions to the annual budgets, largely because of the poorly understood mechanisms of cold-season soil  
 heterotrophic respiration and therefore uncertain numerical representations (Natali et al., 2019; Zona et al., 2016; Wang et  
 al., 2019; Commane et al., 2017). Thus, it remains challenging to assess the response of permafrost carbon dynamics to  
 35 Arctic warming and to predict future annual carbon budgets with current Earth System Models (ESMs).

In ESM land models, soil environment influences soil microbial heterotrophic respiration (HR) and decomposition of soil  
 organic carbon (SOC) mainly through applying prescribed temperature and moisture functions to modify base decomposition  
 rates. These functions, however, rely heavily on empirical or semi-empirical relationships which are highly uncertain (Sierra  
 40 et al., 2017; Sierra et al., 2015; Yan et al., 2018; Moyano et al., 2013; Tang and Riley, 2019; Rafique et al., 2016; Bhanja and  
 Wang, 2020; Kim et al., 2019). Specifically, the temperature sensitivities of soil carbon decomposition is often represented  
 with a  $Q_{10}$  value (i.e., the increase in respiration rate from a 10°C increase in temperature) that is fixed at 1.5 or 2.0 (Meyer  
 et al., 2018). However, the values of  $Q_{10}$  are controversial (Davidson and Janssens, 2006). Some studies found a uniform  $Q_{10}$   
 across biomes and climate zones, e.g., as 1.4 (Mahecha et al., 2010). Other studies demonstrated that  $Q_{10}$  varies with  
 45 environmental conditions, ecosystem types, and soil texture (Meyer et al., 2018; Graf et al., 2011; Kim et al., 2019), showing  
 a large spatial heterogeneity with generally higher values in the high-latitude regions (Zhou et al., 2009). In addition,  
 Wilkman et al. (2018) reported a temporal heterogeneity in  $Q_{10}$  over the Alaskan Arctic Tundra and suggested a higher value  
 (e.g., 2.45) for early summer (e.g., June) but lower value (e.g., 1.58 to 1.67) for the peak growing season (e.g., July).  
 Dynamic decomposition temperature sensitivities are also consistent with theory of microbial dynamics (Tang and Riley,  
 50 2015). Also, the response of HR to changes in soil moisture is commonly expressed by empirical relationships in ESMs,  
 which vary substantially (Sierra et al., 2015; Yan et al., 2018; Moyano et al., 2013). Although in-situ measurements reveal  
 that microbial respiration occurs under very cold conditions (e.g., even when soil temperature is lower than -15 °C) (Natali et  
 al., 2019; Zona et al., 2016), most process-based models completely shut down microbial activity due to limited liquid water  
 in freezing and subfreezing soils, and few modelling studies have closely investigated the HR-moisture relationships in  
 55 frozen conditions.



The strong dependency of CO<sub>2</sub> and CH<sub>4</sub> emission on soil temperature and moisture in ESM land models (Riley et al., 2011; Koven et al., 2017; Lawrence et al., 2015) requires accurate estimates of these two closely related soil variables, especially in cold regions where both increases and decreases in soil temperature could lead to soil “drying” due to drainage or freezing processes. However, current land models tend to significantly underestimate soil temperature during the cold season over permafrost regions (Dankers et al., 2011; Tao et al., 2017; Nicolsky et al., 2007; Yang et al., 2018b). One possible reason is that many land models fail to appropriately account for the latent heat released during soil water freezing (Yang et al., 2018a; Nicolsky et al., 2007). Latent heat released during freezing might be sufficient to offset heat conduction towards the surface, thus maintaining the subsurface soil temperature around the freezing point (i.e., 0°C) for weeks or even months during the fall (i.e., the so-called Zero-Curtain Period; ZCP) (Outcalt et al., 1990). The ZCP conditions allow for continued soil heterotrophic respiration at notable rates, and thus CO<sub>2</sub> and CH<sub>4</sub> production and emissions from subsurface soils (Kittler et al., 2017; Arndt et al., 2019; Commane et al., 2017). For instance, Zona et al. (2016) reported that a substantial portion of cold season CH<sub>4</sub> emissions occurred during the ZCP from Alaskan upland tundra sites. Nevertheless, many land models cannot accurately capture the ZCP length due to their underestimation of soil temperatures, thus underestimating cold-season emissions of CO<sub>2</sub> (Commane et al., 2017) and CH<sub>4</sub> (Zona et al., 2016).

We hypothesize that the underestimation of modelled cold-season CO<sub>2</sub> and CH<sub>4</sub> emissions in ESMs land models primarily results from underestimated soil temperatures during the cold season, the poor representations of environmental controls on heterotrophic respiration in subfreezing soils, and the lack of appropriate representation of cold-season methane transport processes. Here we apply the Energy Exascale Earth System Model (E3SM) land model version 1 (ELMv1-ECA) (Golaz et al., 2019; Zhu et al., 2019) to explore these hypotheses. We apply ELMv1-ECA to (i) improve simulations of subsurface soil temperatures, ZCPs, and CO<sub>2</sub> and CH<sub>4</sub> emissions over the permafrost tundra ecosystem; (ii) investigate the underlying processes that influence cold-season carbon emissions from freezing and subfreezing soils, including source characterization and transport pathways; and (iii) estimate historical trends (from 1950 to present) of cold-season CO<sub>2</sub> and CH<sub>4</sub> emissions at multiple Alaskan tundra sites.

The paper is organized as follows: (1) We describe the study sites and the data used in the study. (2) We present the theoretical background of essential modules of ELMv1-ECA relevant to this study and our modifications to the model’s representations of phase-change, SOC decomposition, and methane dynamics. (3) We then describe the model configuration and experimental design. (4) We assess the modified phase-change scheme by comparing simulated soil temperatures and ZCPs against observations. (5) With the revised phase-change scheme and methane module, we analyze how the decomposition schemes impact simulated CO<sub>2</sub> and CH<sub>4</sub> emissions at the site scale. (6) Finally, we summarize the main findings and discuss needed observations and model development to further improve predictability.



## 2 Study Sites and Data

90 We assembled daily observations of CO<sub>2</sub> and CH<sub>4</sub> fluxes from 2013 to 2017 at five eddy-covariance flux tower sites in Alaska's North Slope tundra (Figure 1) from the Arctic-Boreal Vulnerability Experiment (ABoVE) project (2015 - 2017) (Oechel and Kalhori, 2018) and Carbon in Arctic Reservoirs Vulnerability Experiment (CARVE) flight campaign (2013 - 2014) (Zona et al., 2016). CARVE CO<sub>2</sub> measurements were not available; therefore, monthly winter-time CO<sub>2</sub> flux data at the ABoVE towers assembled by Natali et al. (2019) are included to complement CO<sub>2</sub> observations from 2013 to 2014. The

95 five sites include three eddy covariance (EC) towers at Barrow (i.e., the Barrow Environmental Observatory (BEO) tower, the Biocomplexity Experiment South (BES) tower, and the Climate Monitoring and Diagnostics Laboratory (CMDL) tower), one tower at Atkasuk (ATQ) and another at Iivotuk (IVO) which is located at the foothills of the Brooks Range. BES and CMDL are collocated with each other with sensors installed at different heights (i.e., 2 m for BES and 5 m for CMDL). Vegetation at Barrow is mainly moist acidic tundra. Instrument height at ATQ and IVO is 2 m and 4 m, respectively. ATQ is

100 a well-drained upland site, and the vegetation consists of moist-wet coastal sedge tundra and moist-tussock tundra surfaces. Vegetation at IVO is polar tundra. Table S1 provides basic information including geolocations, vegetation mosaic, and climatologic air temperature at the sites. (Tables numbered with a prefix "S" are include in the supplementary file, which will not be repeated in the following context throughout the manuscript.)

105 ABoVE and CARVE provide soil temperature and moisture measurements at various depths from 5 cm to 40 cm. The Permafrost Laboratory, Geophysical Institute of University of Alaska Fairbanks (GIPL-UAF), provides daily subsurface soil temperature observations down to various depths at permafrost sites across Alaska([http://permafrost.gi.alaska.edu/sites\\_map](http://permafrost.gi.alaska.edu/sites_map)) (Romanovsky et al., 2009). We used the GIPL-UAF permafrost sites that are collocated with the ABoVE sites to complement the ABoVE observations at deeper depths, including BR2 (down to 15 m) and IV4 (down to 1 m). We first

110 filled missing gaps vertically by fitting a polynomial to the soil temperature profile (Kurylyk and Hayashi, 2016) on a daily scale, then screened out outliers by examining the daily time series. Further, we aggregated both the ABoVE and the GIPL-UAF soil temperature measurements to ELMv1-ECA soil layer node depths using the inverse distance weighting method (Tao et al., 2017), and then averaged the two sets of aggregated observations. We used the assembled subsurface temperature observation datasets to evaluate the ELMv1-ECA simulated soil temperature profiles and the zero-curtain periods.

115 Due to the discontinuity of observed soil moisture over time and along with the vertical depth, evaluating ELMv1-ECA simulated liquid water content at layer node-depth was limited. We matched soil-moisture observations to the vertically closest model layer, and then evaluated the simulated volumetric fraction of soil liquid water content at layers for time periods during which observations were available. In addition, we used ABoVE soil moisture measurements to derive site-

120 scale soil porosity and organic carbon content (see Section 3.2).



### 3 Methodology

#### 3.1 Modifications to E3SM Land Model (ELM)

The E3SM land model version 1 (ELMv1-ECA) couples essential biogeophysical and biogeochemical processes that solve terrestrial ecosystem energy, water, carbon, and nutrient dynamics (Golaz et al., 2019; Zhu et al., 2019). Figure 2 illustrates the coupling and interactions among the three components. In the appendix, we describe in detail its subsurface soil thermodynamics, the carbon decomposition module, and the methane module that are of particular relevance to our study. Here we identify the potential problems of ELMv1-ECA that are responsible for the underestimation of cold-season CH<sub>4</sub> and CO<sub>2</sub> emissions and summarize the modifications made to ELMv1-ECA, emphasizing the model enhancements, shown by the ellipses with red boundaries in Figure 2.

##### 3.1.1 Phase Change Scheme

We first improved ELMv1-ECA's numerical representation of coupled water and heat transport with freeze-thaw processes via improving the phase-change scheme. The freeze-thaw processes of soil water within ELMv1-ECA is simulated in a decoupled way, i.e., it solves soil temperatures ignoring the latent heat associated with phase change, determines the mass change of soil water required to adjust the initially solved soil temperature to the freezing point (i.e., 0°C;  $T_f$ ), adjusts the soil liquid and ice content by mass and energy conservation, and then readjusts temperatures after accounting for the heat deduction or compensation resulted from melting or freezing (see the detailed description in the Appendix A). The underlying assumption here is, taking the freezing process as an example, the available liquid water at the initially solved temperature ( $T_i^{n+1}$ ) will be completely frozen, releasing latent heat ( $H_i$ ) to bring up  $T_i^{n+1}$  back to  $T_f$ . Then, the estimated phase-change rate will be tuned down and the current temperature (i.e.,  $T_f$ ) will be readjusted if the to-be-increased ice mass is larger than the required mass change ( $-H_m$ ) (see (Eq. A4) in the Appendix A), which, however, only occasionally occurs. When the liquid water available to be frozen becomes small enough, the released latent heat is not sufficient to compensate for the required energy deficit ( $T_f - T_i^{n+1}$ ), and then the freezing process stops. Consequently, the model freezes soil water quickly, resulting in an underestimated duration of the soil water phase-change processes and the zero-curtain periods, and also cold-biased winter temperatures (Nicolsky et al., 2007; Yang et al., 2018a).

Here, we employed a phase-change efficiency and the temperature of the freezing-point depression to effectively solve the problem of overestimating phase-change rates within the current ELMv1-ECA modelling structure. These modification factors are explained below. The phase-change efficiency, introduced by Le Moigne et al. (2012) and adopted by Masson et al. (2013) and Yang et al. (2018a), introduces the dependency of available liquid water on the phase-change rate (Le Moigne et al., 2012). The phase-change efficiency for freezing,  $\varepsilon_{liq,i}^n$  (see (Eq. A7)), is identical to the degree of moisture saturation, or the volumetric fraction of soil liquid water content (i.e.,  $Sf_{liq,i}^n = \theta_{liq,i}^n / \theta_{sat,i}$  where  $\theta_{liq,i}^n$  is soil liquid water content and



$\theta_{sat,i}$  is porosity). The underlying assumption here is that the liquid water of soil resists freezing as the freezing process proceeds and  $Sf_{liq,i}^n$  decreases, analogous to how dry soils resist getting drier due to capillary force. We applied the phase-change efficiency to the initially estimated energy and mass change involved, i.e.,  $H_i$  and  $H_m$  (see (Eq. A4) in the Appendix)  
 155 when freezing or thawing process occur.

As in Nicolsky et al. (2007) and Yang et al. (2018a), the occurrence of a phase-change process is then determined by the temperature of the freezing point depression (i.e., an virtual temperature, see (Eq. A8)) instead of  $T_f$ . The virtual freezing point depression temperature is reversely derived from the freezing point temperature-depression equation (Fuchs et al.,  
 160 1978; Cary and Mayland, 1972). With an upper limit as  $T_f$ , the virtual temperature describes the lowest temperature that can hold current liquid water content in the freezing soils. That is, the soil temperature has to be lower than the current virtual temperature to allow the freezing process to occur further.

We describe in detail the revised phase-change scheme in the Appendix A. In short, we improved the phase-change scheme of ELMv1-ECA by incorporating two modifications: 1) applying a phase-change efficiency to implicitly account for the heat compensation/deduction to the system from latent heat released/absorbed by soil water freezing/melting, and 2) replacing  
 165 the constant freezing point with the temperature of the freezing point depression, as a virtual temperature, to determine the occurrence of phase change in subfreezing soils.

### 3.1.2 Environmental Modifiers to the Decomposition Rate

We revisited ELMv1-ECA's representation for soil heterotrophic respiration dynamics in subfreezing soils and then scrutinized the environmental scalars of soil temperature and moisture. Within ELMv1-ECA's decomposition cascade model, the environmental factors that impact the decomposition rates of soil organic matter include soil temperature ( $f_T$ ), soil moisture ( $f_W$ ), oxygen stress ( $f_O$ ) and a depth scalar ( $f_D$ ) (See Appendix B). Within freezing and subfreezing soils, the soil water potential is related to temperature through the freezing point depression equation (Niu and Yang, 2006). The  
 175 current moisture factor  $f_W$ , therefore, can predict zero respiration rates for subfreezing soils given a minimum soil water potential  $\psi_{min}$ , as shown by Figure S1a in the supplementary file. (Figures numbered with a prefix "S" are include in the supplementary file, which will not be repeated in the following context throughout the manuscript.) We thus imposed a minimum threshold ( $f_{W,min}$ ) to prevent zero respiration within the active layer when soil becomes subfreezing during cold-season months (Figure S1b).

180

For wet soils, the factor that primarily limits the decomposition rates is oxygen availability (Sierra et al., 2017), since increases in soil moisture result in decreased dissolved oxygen. ELMv1-ECA approximates oxygen stress ( $f_O$ ) as a ratio of available oxygen to the demand by decomposers, which, however, is highly uncertain and unstable (Oleson et al., 2013).



Adapting the concept and formulation of Yan et al. (2018), we incorporated oxygen stress into the moisture scalar to account for the inhibition of decomposition in wet anoxic conditions. The revised form of the moisture scalar  $f_W^*$  (Eq. B11) gradually decreases when the degree of saturation exceeds an optimal wetness threshold ( $Sf_{op}$ ) that represents the most favorable soil moisture condition for decomposition, as shown by Figure S1b. We also tested several modified moisture schemes with different shape parameters ( $b$  in Eq. B11) and optimal wetness thresholds and minimum thresholds ( $Sf_{op}$  and  $f_{W\_min}$  in Eq. B11). When using the modified moisture scalar with the built-in oxygen stress, the total environmental impacts on decomposition, i.e.,  $f_{total} = f_T f_W f_O f_D$  will be modified accordingly as  $f_{total} = f_T f_W f_D$  to avoid double-counting of the oxygen stress.

ELMv1-ECA uses a  $Q_{10}$ -based standard exponential function to account for the temperature effect on SOC decomposition (Eq. B9), with  $Q_{10}$  as 1.5 and  $T_{ref}$  as 25°C. Here, rather than striving for a single value of  $Q_{10}$ , or a spatial map of  $Q_{10}$  as discussed in the introduction, we seek an optimized scheme at the site scale and a generic scheme at the regional scale for the total environmental modifier ( $f_{total}$ ) that combines moisture ( $f_W$ ) and temperature ( $f_T$ ) sensitivity. Specifically, we assembled and tested 200 cases of  $f_{total}$  using the newly modified moisture scalars with different parameters  $b$ ,  $Sf_{op}$ , and  $f_{W\_min}$ , temperature scalars with different values of  $Q_{10}$  and  $T_{ref}$ , and a variety of other empirical moisture and temperature functions, as documented by Sierra et al. (2015). A full list of the specific moisture and temperature scalars used is provided in Table S2.

### 3.1.3 Cold-season Methane Process

The ELMv1-ECA methane model solves the reaction and diffusion equation for  $CH_4$  and  $O_2$  fluxes with the Crank-Nicholson method. It includes the representations of  $CH_4$  production, oxidation, and three pathways of transport, including aerenchyma tissues, ebullition, aqueous and gaseous diffusion (Riley et al. (2011)). A short description of the ELMv1-ECA methane module is provided in Appendix C. The ELMv1-ECA methane model has been found to underestimate cold-season methane emissions over northern wetlands (Xu et al., 2016). The modifications to the phase-change scheme impact simulations of soil water and heat transfer (3.1.1); the changes in environmental scalar affect substrate availability (3.1.2). Both (3.1.1) and (3.1.2) influence carbon decomposition and soil heterotrophic respiration (Figure 2), and could potentially lead to improvements in simulated  $CO_2$  and  $CH_4$  production, but not necessarily  $CH_4$  emissions which are also controlled by transport mechanisms (Figure 2). Thus, we further refined the cold-season methane transport processes.

Here, we first modified the ELMv1-ECA  $CH_4$  transport mechanism in cold seasons by mimicking possible pathways for  $CH_4$  emissions from freezing and subfreezing soils. Specifically, we mimic the emissions from ice cracks by plant aerenchyma transport (Zona et al., 2016), approximating the gas diffusion through ice cracks to the similar mechanism of diffusion through the aerenchyma tissues. Although in-situ experiments demonstrated that during winter, produced  $CH_4$  in



frozen soils is predominately emitted to the atmosphere through vascular plants aerenchyma tissues (e.g., Kim et al., 2007), here we integrate the possible transport pathways including ice cracks and remnants of aerenchyma tissues together through equation (Eq. C14).

220 During the cold season over the tundra ecosystem, snow on the land surface provides strong resistance to CH<sub>4</sub> transport to the atmosphere in ELMv1-ECA, as shown in Figure 2. But in reality, studies have shown methane can diffuse through snowpack at varying rates (Kim et al., 2007). We thus decreased snow resistance at the upper boundary by introducing a new scale factor when snow is present. Also, in ELMv1-ECA, the aqueous diffusion coefficients in freezing and subfreezing soils below the water table are based on the volumetric fraction of the liquid water content, which is quite small (i.e., the  
 225 supercooled liquid water) and thus limits diffusion. We revised the formulation (Eq. C15), assuming a higher scaling factor for frozen soils ( $f_{frzsoil}$ ) upon sensitivity experiments (not shown). Table 1 summarized all the specific modifications made to ELMv1-ECA. These modifications involve new parameters that are all tuneable and can be systematically optimized via calibration. Here, we seek to reproduce the first-order cold-season process relevant to this study with these default formation and values listed in Table 1.

### 230 3.2 Climate Forcing, Model Configuration, and Experiment Design

We conducted transient simulations at 30-minute temporal resolution driven by climate forcing from 0.5°×0.5° CRU JRA (Harris, 2019) from 1901 to 2017 at the four Alaska tundra site locations. Before the transient simulation, we conducted a 200-year Accelerated Decomposition (AD) spin-up period followed by a 200-year regular spin-up period (Koven et al., 2013b; Zhu et al., 2019) to initialize land carbon pools. Spin-up simulations start from a wet and cold condition. Specifically,  
 235 sub-surface temperatures were initialized as 274 K for the 1<sup>st</sup> to 5<sup>th</sup> soil layers, 273 K for the 6<sup>th</sup> to 10<sup>th</sup> layer, and 272 K for the 11<sup>th</sup> to the 15<sup>th</sup> layer, and volumetric soil water content was initialized fully saturated for all layers. In this manner, consistent vertical soil water content profiles were built in over the permafrost regions.

Baseline simulations were conducted with ELMv1-ECA default physics, parameters, and surface datasets, i.e.,  
 240 OriPC\_OriDecom\_OriCH4 using original phase-change scheme, original decomposition scheme and methane module (Table 2). To improve the model representation of the site-level soil environment, we first examined the global soil organic matter data at the ABoVE sites by evaluating ELMv1-ECA simulated subsurface soil temperature with the topsoil temperature prescribed to observations (as did in Tao et al., 2017). Using the top soil layer as the upper boundary, the modelling system excluded potential errors induced by inaccurate meteorological forcing and vegetation cover that impact the simulation of  
 245 heat transfer from the atmosphere to the shallow soil (Tao et al., 2017). Then, the accuracy of simulated soil subsurface temperature is directly determined by the factors impacting heat transfer along the “shallow-to-deep soil” gradient (Koven et al., 2013a), e.g., soil thermal properties which are mostly determined by SOC content (Tao et al., 2017; Lawrence and Slater, 2008). Results well reproduced the subsurface soil temperatures except at IVO, where summer soil temperatures were





notably overestimated (see Figure S2a). This result indicates that the SOC content at IVO was too small, leading to a large thermal conductivity, small soil porosity, and small heat capacity, altogether resulting in fast penetration of heat into the subsurface soil during summer (Tao et al., 2017; Lawrence and Slater, 2008). Thus, we derived the organic matter density at IVO based on ABoVE soil moisture data through a linear relationship between SOC content and soil porosity (i.e., Equation 3 in Lawrence and Slater (2008)), assuming the observed maximum volumetric water content was porosity (see Figure S3 for details). With the newly derived profile of soil organic matter density at IVO, the simulation showed large improvements in summer soil temperatures compared to that using the original global carbon dataset (see Figure S2b). The derived SOC content is also consistent with the soil survey data reported in Davidson and Zona (2018). Hereafter, the simulations at IVO presented in this paper use the newly derived organic carbon data without repeated clarification.

The representative spatial scale of the eddy flux tower is small compared to the grid cell of global surface datasets and the climate forcing data used by ELMv1-ECA, although the forcing dataset was interpolated to the site scale with a bilinear or nearest-neighbor method. The site-scale vegetation cover also shows a large diversity of vegetation types according to the detailed vegetation survey at ABoVE flux tower footprints obtained in 2014 (Davidson and Zona, 2018). We analyzed the vegetation composition from the closet survey plot to the flux tower and examined the rationality of ELMv1-ECA's percentage of plant type function (PFT) for the site-scale simulation. We confirmed that ELMv1-ECA's PFT dataset was a good compromise between representing the site-scale ecosystem and other global parameters and surface datasets within ELM. The simulated saturated and unsaturated CH<sub>4</sub> emissions were weighted with the estimated inundation fractions at the footprint of ABoVE eddy-covariance flux towers (see details in (Xu et al., 2016)) in order to compare simulated CH<sub>4</sub> emissions with ABoVE measurements at the site scale.

Table 2 lists the experiments conducted in this study. We modified each model component (i.e., the heat transfer model, carbon decomposition model, and methane model) serially. For the temperature- and moisture-dependency functions, we analyzed 200 environmental modifiers within the carbon decomposition module and identified an optimal scheme for each site and a generic scheme that can be applied for the regional simulation over Alaskan North Slope tundra (see next section).

### 3.3 Evaluation Method and Trend Analysis

We define the early cold season as September and October, the cold-season period as September to May which includes the two shoulder seasons (both thawing and freezing) as consistent with Zona et al. (2016), and the warm season from June to August. We define the zero-curtain period (ZCP) as the set of successive days when the soil temperature is within the range of  $[-0.75^{\circ}\text{C}, 0.75^{\circ}\text{C}]$  starting in fall (i.e., the freezing season) based on Zona et al. (2016). We computed the ZCP duration for each soil layer every year from 1950 to 2017 and estimated the historical trend as the regression slope between ZCP duration and time. Similarly, we estimated the trends of cold-season CH<sub>4</sub> and CO<sub>2</sub> emissions through linear regression



analysis. A p-value of 0.05 is used to determine if the computed trend is statistically significant. Results vary with soil depths; thus, we choose a common modelling depth, i.e., 12 cm, which locates within the active layer for all the sites, to give an example.

285

We used Nash-Sutcliffe Efficiency (NSE) (Nash and Sutcliffe, 1970) to examine the performance of the ELMv1-ECA simulated time series of CH<sub>4</sub> and CO<sub>2</sub> net fluxes in comparison with assembled observations (Section 2) at the monthly time scale. The NSE ranges from negative infinity to one, calculated as Eq. (1):

$$NSE = 1 - \left( \frac{1}{N} \sum_{t=1}^N (\hat{E}_t - O_t)^2 \right) / \sigma_o^2, \quad (1)$$

where  $t$  means monthly time step,  $N$  is the total number of time steps,  $\hat{E}_t$  and  $O_t$  is simulated and observed flux at time step  $t$ , respectively; and  $\sigma_o$  is the standard deviation of observations. Note we only used observed monthly averages when the number of daily observations was more than 20 days. The model performance is generally considered satisfactory with an NSE > 0.50 (Moriassi et al., 2007), and perfect with an NSE as one. To simultaneously evaluate CH<sub>4</sub> and CO<sub>2</sub> fluxes, we combined both  $NSE_{CH_4}$  and  $NSE_{CO_2}$  in the form of  $dist = \sqrt{(1 - NSE_{CH_4})^2 + (1 - NSE_{CO_2})^2}$ , representing the distance from  $(NSE_{CH_4}, NSE_{CO_2})$  to (1, 1) in a coordinate plane with x-axis as  $NSE_{CH_4}$  and y-axis as  $NSE_{CO_2}$ . The optimal simulation thereby is the one having the shortest distance to the ideal scenario (1, 1). We also define a satisfactory model performance in terms of simulating CH<sub>4</sub> and CO<sub>2</sub> fluxes as the case with both  $NSE_{CH_4}$  and  $NSE_{CO_2}$  larger than 0.5. The generic scheme then is the common satisfactory scheme that provides the best overall performance for all the sites.

To evaluate ELMv1-ECA simulated soil temperature and moisture, we calculated the RMSE for each soil layer, i.e.,  $\sqrt{\sum_{t=1}^N (\hat{E}_t - O_t)^2 / N}$  where the  $\hat{E}_t$  and  $O_t$  is simulated and observed soil temperature or moisture, respectively, and  $t$  is a daily time step. We used the Mean Absolute Error (MAE, i.e.,  $\frac{1}{N} \sum_{t=1}^N |\hat{E}_t - O_t|$ ) to assess the simulated duration of ZCP of each soil layer. Note that, depending on the amount of soil liquid water content, the whole course of the freezing process may or may not entirely fall into the ZCP, i.e., the ending time of ZCP does not necessarily align with the end of the freezing process. The onset of freezing, though, is always later than the starting day of the ZCP, and the main course of the freezing process is still within the ZCP.

Here the modelled active layer thickness (ALT), i.e., maximum thaw depth during an annual cycle, is computed as the bottom depth of the deepest thawed soil layer (i.e., with a maximum annual temperature above 0°C) further extended down to the possible non-frozen fraction of the layer below, as in Tao et al. (2019; 2017). We only derived the length of ZCP for soil layers with a maximum annual temperature above 0°C since limited phase-change processes occur in deeper layers. Then, the soil layers containing or below the permafrost table have a zero-day ZCP. We computed the MAE of ALT



simulated with both original (OriPC) and the new phase-change (NewPC) scheme. Also, we computed the relative improvement in simulated soil temperature (Ts) and ZCP compared to the baseline results. Specifically, we calculated  $100\% \times (\text{RMSE\_Ts\_OriPC} - \text{RMSE\_Ts\_NewPC}) / \text{RMSE\_Ts\_OriPC}$  and  $100\% \times (\text{MAE\_ZCP\_OriPC} - \text{MAE\_ZCP\_NewPC}) / \text{MAE\_ZCP\_OriPC}$  to quantify the enhancement by employing the new phase-change scheme.

In general, we use NSE to evaluate the model's performance in capturing seasonality (i.e., time series of CH<sub>4</sub> and CO<sub>2</sub> net fluxes) and use RMSE and MAE to assess the model's capability in simulating the magnitudes of soil temperature, moisture saturation, and ZCP durations.

## 4 Results and Discussion

### 4.1 Evaluation of Soil Temperature and Zero-curtain Period

We first evaluated the simulated daily soil temperature profiles against the observations from ABoVE and GIPL-UAF at the four site locations. Then, we examined improvements in simulations of soil temperature, soil moisture, and the durations of ZCPs by employing the newly revised phase-change scheme (i.e., "NewPC\_OriDecom\_OriCH4"; Table 2).

Results for the BES/CMDL and IVO site are shown in Figure 3; results for other sites are shown in supplementary Figure S4. At BES/CMDL, the baseline (i.e., "OriPC\_OriDecom\_OriCH4"; Table 2) simulated soil temperatures (Ts) with the default phase-change scheme (Ts\_OriPC; cyan lines; Figure 3a) decrease rapidly in fall due to the overestimated freezing rate (i.e., the slope of decreasing liquid water fraction), notably underestimating the duration of the ZCP (greenish shaded area). Consequently, liquid water saturation (S<sub>f</sub>\_OriPC, green lines; Figure 3a) quickly drops to a lower bound (i.e., the supercooled liquid water content divided by porosity), and the freezing process generally completes within a short period (days for top layers to one month at the most for deeper layers). The baseline model soil temperature drops (Ts\_OriPC) sharply after the freezing process ends (i.e., S<sub>f</sub>\_OriPC decreases to the lower bound). In contrast, the new phase-change scheme effectively slows freezing rates, showing relatively smaller slopes of decreasing liquid water saturation (S<sub>f</sub>\_NewPC; magenta lines; Figure 3a) within the ZCPs than the baseline simulation (S<sub>f</sub>\_OriPC; green lines) especially in the 4<sup>th</sup> and 5<sup>th</sup> layer. Hence, the gradually released latent heat maintains soil temperatures around the freezing point for a longer period (Ts\_NewPC; blue lines; Figure 3a), effectively extending the ZCPs (blue shaded area) which agree better with observations than the baseline results. The ZCP duration increases with depth and can extend into December for deep soil layers. Similarly improved performance was found at the BEO and ATQ sites (supplementary Figure S4). At IVO, however, while the new phase-change scheme greatly improved simulated results relative to the baseline simulation (Figure 3b), the model still slightly underestimated ZCP durations and also underestimated winter (December to April) soil temperature (blue vs. red). This result at IVO is consistent with the underestimation of late-season soil liquid water available to be frozen, and thereby to release sufficient latent heat (Figure S5).



345 Simulated ZCP durations with the revised phase-change scheme (NewPC) demonstrated notable improvements over the  
 baseline (original) phase-change scheme (OriPC) (solid circles vs. open diamonds) (Figure 3), showing greatly reduced  
 mean absolute errors (MAEs) (Table 3). For example, at 12 cm depth (4<sup>th</sup> layer), the relative improvements in MAE of the  
 ZCP durations were 65%, 65%, 66%, and 50% for the four site locations (Table 3). The largest improvement in MAE was as  
 large as 65 days for the 6<sup>th</sup> layer at BES/CMDL, with a relative improvement of 84% (Table 3). This large improvement  
 350 stems from the better-estimated ALT at this site; the OriPC simulated 6<sup>th</sup> layer temperature remained below freezing, leading  
 to a zero-day ZCP (diamonds on the x-axis in Figure 4). The new phase-change scheme not only improved simulation of the  
 ZCP and cold-season soil temperatures, but also affected the warm season dynamics and thus ALT estimates. As Figure 4  
 indicates, the NewPC improved simulated ALTs at all four site locations with reduced bias in multi-year averaged ALT,  
 resulting in more reasonable ZCP durations for the 6<sup>th</sup> layer (and also 7<sup>th</sup> layer for IVO), while the baseline results were zero  
 355 days.

The deeper active layer simulated by NewPC implies more soil water storage capacity, resulting in lower soil moisture in  
 shallow soil layers and higher soil water in deep layers ( $S_{f\_NewPC}$ ; magenta lines; Figure 3) compared to baseline results.  
 The changes in soil liquid water content, in turn, impact phase-change and soil temperature simulations. Comparison with  
 360 the observed soil liquid water content reveals a better agreement with observations (Table S3). For example, at ATQ (Figure  
 S6), the RMSEs of the liquid water content were reduced by 5.4%, 35.3%, 42.6%, and 25.4% for the 3<sup>rd</sup> through 6<sup>th</sup> layers,  
 respectively (Table S3).

The changes to model representations of phase change led to large reductions in soil temperature bias. The relative  
 365 improvements in RMSE of simulated soil temperatures during Sep. and Oct. (i.e., the two months that the ZCPs usually  
 cover), generally increased with depth for surface layers (within about 20 cm of the surface, i.e., 1<sup>st</sup> to 4<sup>th</sup> layer), and were  
 above 80% for the intermediate layers (5<sup>th</sup> to 8<sup>th</sup>) at all the sites (Figure 5). At the two Barrow sites where observed soil  
 temperatures were available, the relative improvements for the deepest (13<sup>th</sup>) layer were 72.6% and 71.1%, on average, for  
 the early winter and annual cycle, respectively. Therefore, incorporating the new phase-change scheme also resulted in  
 370 improved bottom temperature boundary conditions, which is critical for accurately simulating permafrost dynamics (Sapri-  
 Azuri et al., 2018). Improvements between September and December and the whole annual cycle also increased with soil  
 depth, showing site-averaged reductions in RMSEs ranging from 47% to 63% and from 36% to 46% for the two periods,  
 respectively. The whole cold-season period (Sep. to May) showed, on average, 44% to 53% reduction in RMSEs from the 1<sup>st</sup>  
 to 6<sup>th</sup> layer at relatively warmer sites (i.e., ATQ and IVO), and from 19% to 69% for the top 13 layers for the two Barrow  
 375 sites.



Soil temperatures were still slightly underestimated during the thawing season (i.e., May) at all four sites, showing later onset of thawing indicated by the timing when warming soil temperatures cross 0°C and soil moisture starts to rise (Figure 3). One possible reason for this bias is the lack of representation of advective heat transport. That is, the model does not represent the heat of spring rain that is advectively transported into soils (Neumann et al., 2019; Mekonnen et al., 2020); nor does it account for advective heat transport associated with water fluxes in subsurface soils after the spring-rainwater mix with existing cold liquid water in soils. Also, after the freezing process ends, simulated deeper soil layer temperatures were underestimated (e.g., December through April). This bias might be caused by underestimated snow depth (not shown) resulting from inaccurate forcing (particularly snowfall), land cover, microtopography, and/or wind-blown snow redistribution.

The improved simulations of soil temperature, liquid water content, and ZCP duration greatly impacted soil HR and methane production (Figure 6). Increases in the baseline modeled HR and CH<sub>4</sub> production resulted from changes in soil temperature and moisture (Figure 6b1 and b2 vs. Figure 6c1 and c2) and mainly occurred within the two-dimensional “zero-curtain zone” across the vertical soil profile spanning multiple months, i.e., from September to November (Figure 6c1). However, still very small HR and CO<sub>2</sub> and CH<sub>4</sub> production were predicted during the following cold season months (Figure 6c3 and c4) due to the moisture scalar for subfreezing soils estimated by ELMv1-ECA’s original moisture-dependency function on decomposition (Eq. B10), as discussed in Section 3.1.2. In addition, the sharp decreases of HR and CH<sub>4</sub> production around the end of September were caused by the dramatically increased oxygen stress (i.e., the decreased oxygen scalar) to decomposition when freezing began (Figure 6c3 and c4). By replacing the original moisture scalar with the modified soil moisture-dependency function scheme-2 with oxygen stress ((Eq. B11), also see Figure S1) along with the modified total environmental modifier, both the near-zero respiration and sharp drawdown trends in HR and CO<sub>2</sub> and CH<sub>4</sub> production were greatly alleviated (Figure 6c3 and c4 vs. Figure 6d3 and d4). In the next section, we analyze 200 environmental modifier schemes to the base decomposition rate (Table S2) that assembled commonly used empirical soil temperature- and moisture-dependency functions as documented by Sierra et al. (2015) and the modified functions proposed in this study.

## 4.2 Evaluation of CO<sub>2</sub> and CH<sub>4</sub> Emissions

Here we evaluate the simulated monthly CO<sub>2</sub> and CH<sub>4</sub> fluxes at the site scale against EC tower observations. Figure 7 displays the NSEs of 200 ELMV1-ECA ensemble simulations with different combination of temperature and moisture scalars on soil decomposition, i.e., “NewPC\_NewDecom\_NewCH<sub>4</sub>” (grey dots) (see configurations in Table 2). (Daily time series of all the simulations are provided in Figure S7). The failure of simulated CH<sub>4</sub> emissions to capture the methane seasonality at IVO (as indicated by Figure S7) might occur because of the lack of 1) a reasonable wetland module that can adequately account for inundated hydro-ecological dynamics, 2) advective heat transport at the air-ground interface through rainfall infiltration and within subsurface soils through water transfer, and 3) the geological micro-seepage emission of CH<sub>4</sub>,



as reported in previous studies (Anthony et al., 2012; Etiope and Klusman, 2010; Russell et al., 2020). For instance, Lyman et al. (2020) showed large temporal variability of CH<sub>4</sub> at natural gas well pad soils, similar to the observations at IVO (Anthony et al., 2012). Controlled experiments (not shown) that imposed observed soil temperature and moisture into the modelling system at all the layers with observations available do not demonstrate improvement for the simulation of CH<sub>4</sub>, although showing better performance for CO<sub>2</sub>. These results confirm that impacts from the soil environment (e.g., soil temperature and moisture) within the current water and heat transfer framework cannot explain the seasonal variability of CH<sub>4</sub> emissions. Thus, the three mechanisms discussed above (i.e., wetland dynamics, advective heat transport, and geological micro-seepage CH<sub>4</sub> emission) currently missing in our model are likely necessary to simulate CH<sub>4</sub> emissions at this site and we therefore do not include analysis at IVO in the following sections.

The improved phase-change scheme, and thus improved simulations of ZCP durations and soil temperature and moisture, resulted in greatly improved performance for CO<sub>2</sub> emissions at BES/CMDL and BEO, and slightly better performance for CH<sub>4</sub> emissions at ATQ, compared to the baseline (cyan for “NewPC\_OriDecom\_OriCH<sub>4</sub>” vs. green for baseline; Figure 7), even though the carbon decomposition and methane modules remained the same. Incorporating the revised CH<sub>4</sub> model (discussed in section 3.1.3) improved simulated CH<sub>4</sub> emissions at BES/CMDL, BEO, and ATQ (blue for “NewPC\_OriDecom\_NewCH<sub>4</sub>” vs. cyan for “NewPC\_OriDecom\_OriCH<sub>4</sub>”), especially during the cold season (Figure 8). The improved NSEs for CH<sub>4</sub> emissions mainly resulted from increased emissions over early winter (Sep. and Oct.) and slight but persistent enhancements throughout the rest of the cold season (blue in Figure 8), which were related to our modifications to CH<sub>4</sub> transport mechanisms. Further, with the identified optimal scheme of environmental modifiers to the base decomposition rate, results demonstrate substantial improvements to the simulation of cold-season CO<sub>2</sub> and CH<sub>4</sub> emissions compared to baseline results (yellow vs. others; i.e., shortest distance from ( $NSE_{CH_4}$ ,  $NSE_{CO_2}$ ) to (1, 1)). Among the common schemes providing good performance for both CO<sub>2</sub> and CH<sub>4</sub> emissions (i.e., both  $NSE_{CH_4}$  and  $NSE_{CO_2}$  larger than 0.5, indicated by the gray dots within the boxes in Figure 7), we identified a generic scheme of environmental modifier to the decomposition rate by selecting the common scheme that provided best overall performance for all the sites (except IVO). The specific functions for the optimal and generic scheme of environmental modifiers are provided in Table S4.

Figure 8 illustrates the uncertainty associated with the model representations of environmental influences on heterotrophic respiration. Most simulations within the grey area (corresponding to the grey dots within the good-performance boxes in Figure 7) employed the modified ELMV1-ECA moisture scalar and the Q<sub>10</sub>-based temperature scalar, differing from each other by using different parameter values (e.g., Q<sub>10</sub>,  $Sf_{op}$ , and  $b$ ). At ATQ, the site with the thicker active layer, results from simulations using moisture-dependency functions documented in Sierra et al. (2015) (Table S2 and Figure S1) were notably different than those using the moisture scalar of ELMv1-ECA. For the Sierra et al. (2015) empirical moisture functions, the influence of liquid moisture content on heterotrophic respiration is uniformly applied to all active soil layers, even though the soil properties are quite different vertically. ELMv1-ECA’s moisture scalars (including the original scheme), in contrast,



reasonably explained the varying influence along the vertical soil profile. Thus, the simulations with moisture functions  
 445 documented in Sierra et al. (2015) (i.e., different than the improved ELMV1-ECA moisture scalar) generally overestimated  
 CO<sub>2</sub> and CH<sub>4</sub> emissions, especially during the warm season when the thaw depth is deep and soil wetness is high, thus  
 permitting large moisture modifier scalar applied to the base decomposition rates.

Both the optimal and the generic decomposition scheme used the modified ELMv1-ECA moisture scalar (see Table S4),  
 450 which assigns small thresholds for the moisture scalar and also incorporates oxygen stress when soil wetness exceeds a  
 favourable threshold (0.65 here) for decomposition. Imposing small thresholds for moisture scalar effectively prevents the  
 possibility of zero respiration in subfreezing soils during wintertime. This change exerts more impact on cold sites, such as  
 the two Barrow sites, due to the smaller supercooled liquid water under the colder temperature. Thus, the improved NSEs for  
 CO<sub>2</sub> and CH<sub>4</sub> emissions at BES/CMDL and BEO were larger than those at ATQ (Figure 7; yellow or magenta vs. blue).  
 455 Since the temperature at ATQ was not cold enough to make the supercooled liquid water content small enough to give a zero  
 moisture scalar, the microbial respiration was not completely shut down with the original decomposition modifier at this site.  
 Indeed, at ATQ, where cold-season temperatures are relatively warmer than at BES/CMDL and BEO, simulations with the  
 original ELMv1-ECA environmental modifier (i.e., “NewPC\_OriDecom\_NewCH4”; discussed in Section 3.1.2), already  
 released much more CO<sub>2</sub> and CH<sub>4</sub> throughout the cold season than in the baseline simulations, owing to the improved  
 460 simulations of soil temperature and moisture, and the modifications for CH<sub>4</sub> transport.

The Q<sub>10</sub>-based temperature functions mediate the response of microbial respiration more over the warm season than the cold  
 season due to the larger sensitivity of heterotrophic respiration to warm temperatures than to subfreezing temperatures (see  
 Figure S1d). The different SOC decomposition Q<sub>10</sub> values employed directly impact soil HR and thus CH<sub>4</sub> and CO<sub>2</sub>  
 465 emissions, and also indirectly impact vegetation nutrient assimilation and thus primary productivity (Figure 2). Vegetation  
 growth, on the other hand, impacts CH<sub>4</sub> emissions because the CH<sub>4</sub> component transported to the surface via vegetation  
 aerenchyma tissue generally dominates the total emissions and thus determines the seasonal peak and general seasonality of  
 CH<sub>4</sub> emissions. When temperature is below the reference temperature (i.e.,  $T_{ref}$ , here is 25°C), a smaller Q<sub>10</sub> permits larger  
 HR and produces more CH<sub>4</sub> and CO<sub>2</sub>, increases warm-season CO<sub>2</sub> uptake via photosynthesis; and increases belowground  
 470 biomass and aerenchyma tissue and thereby CH<sub>4</sub> transport to the atmosphere. Thus, the seasonality of CH<sub>4</sub> and CO<sub>2</sub> net  
 emissions are closely linked through vegetation primary productivity, which vary from site to site. For cold sites (i.e.,  
 BES/CMDL and BEO), the sensitivity of simulated CH<sub>4</sub> to Q<sub>10</sub> values is larger than the sensitivity of CO<sub>2</sub> net flux to Q<sub>10</sub>  
 because cold temperature suppresses vegetation growth (i.e., CO<sub>2</sub> uptake); while for the warm site (i.e., ATQ), both CH<sub>4</sub> and  
 CO<sub>2</sub> net flux are very sensitive to the Q<sub>10</sub> values. Summarizing, the cold sites (i.e., BES/CMDL and BEO) better match CO<sub>2</sub>  
 475 and CH<sub>4</sub> emissions observations with smaller Q<sub>10</sub> values (1.7 or 1.8) than for the warmer site (i.e., 2.1 for ATQ; Table S4).  
 The generic decomposition scheme used a Q<sub>10</sub> value of 2.0, which provided the best overall performance at all three sites  
 (Table S4).



The extended ZCPs, the revised environmental modifier to decomposition, and the modified cold-season CH<sub>4</sub> transport mechanism, together resulted in the largest improvements for both CO<sub>2</sub> and CH<sub>4</sub> emissions, especially over the cold season. In the next section, we quantify the cold season contribution of CO<sub>2</sub> and CH<sub>4</sub> emissions and then estimate the historical trends of seasonal CO<sub>2</sub> and CH<sub>4</sub> emissions from 1950 to 2017.

### 4.3 Cold-season Contribution of CH<sub>4</sub> and CO<sub>2</sub> net emissions and Historical Trends

To better verify the cold-season contribution of CH<sub>4</sub> and CO<sub>2</sub> emissions to the annual budget, a multi-year average approach was taken because of discontinuity in the observed time series. The new simulation results with the optimal decomposition scheme (yellow; Figure 9) showed greatly enhanced performance at three of the study sites in terms of capturing the averaged seasonal cycle, especially for the cold-season months (Sep. to May; Figure 9), reducing site-averaged MAEs in cold-season total CH<sub>4</sub> and CO<sub>2</sub> emissions by 84% and 81%, respectively. Specifically, compared to baseline results, the new simulation results showed 0.94 gC m<sup>-2</sup> and 55.6 gC m<sup>-2</sup> increases in site-averaged cold-season CH<sub>4</sub> and CO<sub>2</sub> emissions, respectively. The observed cold-season CH<sub>4</sub> emissions contributed at least ~40% to the annual total at three of the study sites, of which about half occurred in September and October (Figure 10, Table 5), i.e., the two months hosting the major part of ZCPs for the top to intermediate soil layers. The simulated percentage of cold-season contributions to the annual totals were close to observed values, i.e., 38%, 41%, 28% vs. 45%, 42%, 45% for BES/CMDL, BEO, and ATQ, respectively. The simulated contribution of early cold season (Sep. and Oct.) CH<sub>4</sub> emissions to the cold-season total was 62%, 52%, and 60% for the three sites, in comparison with the observed 47%, 58%, and 43%, showing slightly overestimations.

The new simulations accurately captured the observed cold-season contributions of both CH<sub>4</sub> and CO<sub>2</sub> emissions (Table 5), and the model improvements were larger for cold sites (i.e., BES/CMDL and BEO) than for the warmer site (i.e., ATQ), as discussed above. Specifically, at ATQ, despite the small biases in the annual total CH<sub>4</sub> emission (i.e., -0.16 gC m<sup>-2</sup>) and the early cold season component (i.e., -0.05 gC m<sup>-2</sup>), the new simulation underestimated the cold-season proportion of annual emissions, i.e., simulated 28% vs. observed 45%. In contrast, biases in contribution percentages were only 2% and 7% at BES/CMDL, and 3% and 1% at BEO for the early cold season and cold-season period, respectively. The updated ELMv1-ECA also provided improved cold-season CO<sub>2</sub> emissions, showing small biases of -2.44 gC m<sup>-2</sup> (3% of the observation) and -1.5 gC m<sup>-2</sup> (2% of the observation) for BES/CMDL and BEO, respectively. Compared to BES/CMDL and BEO, results for ATQ showed relatively larger bias of -23.9 gC m<sup>-2</sup> (41% of the observation). The observed multi-year averaged annual CO<sub>2</sub> net flux was 19.9 gC m<sup>-2</sup> (source), 31.8 gC m<sup>-2</sup> (source), and -3.8 gC m<sup>-2</sup> (sink) at BES/CMDL, BEO, and ATQ, respectively. However, due to the large discontinuity in CO<sub>2</sub> observations, especially over the warm season (Figure 8), the calculated annual CO<sub>2</sub> budget is uncertain. Still, we can characterize the CO<sub>2</sub> budget with simulated results using the updated ELMv1-





ECA. We find that the simulated cold-season  $\text{CO}_2$  emissions were larger than the warm-season  $\text{CO}_2$  net uptake at all three sites (Figure 10, Table 5). The released  $\text{CO}_2$  over the early cold season (September and October) accounted for 54%, 50%, and 72% of the total emissions throughout the cold season for BES/CMDL, BEO, and ATQ, respectively.

515 Through trend analysis between 1950 and 2017, we found that the ZCP durations showed increasing trends at all three sites, with ZCP trends increasing with depth (Table 6). At ATQ, a warmer site than BES/CMDL and BEO, the trends of ZCP durations increase from 0.14 to 0.49 days  $\text{yr}^{-1}$  along the vertical soil profile. The  $\text{CO}_2$  emissions during the 12 cm ZCP and during cold-season months (September to May) both showed increasing trends at all three sites (Table 7), ranging from 0.19 to 0.26  $\text{gC m}^{-2} \text{yr}^{-1}$  for the 12 cm ZCP, and from 0.33 to 0.38  $\text{gC m}^{-2} \text{yr}^{-1}$  for the entire cold season period. The annual  $\text{CO}_2$   
 520 net flux showed positive trends, but they were not statistically significant. Annual  $\text{CH}_4$  emissions showed an increasing trend at ATQ with a rate of 10.6  $\text{mgC m}^{-2} \text{yr}^{-1}$ , but not at the two Barrow sites; cold-season  $\text{CH}_4$  emissions did not show significant trends at all the sites. In a companion paper, we discuss the regional trends of the spatially averaged  $\text{CO}_2$  emissions simulated by the updated ELMv1-ECA with the identified generic decomposition scheme.

## 5 Summary and Discussion

525 In this study, we improved ELMv1-ECA simulated subsurface soil temperature, zero-curtain period durations, and cold-season  $\text{CH}_4$  and  $\text{CO}_2$  net emissions at Alaskan North Slope tundra sites. We first improved the numerical representation of coupled water and heat transport with freeze-thaw processes via modifying ELMv1-ECA's phase-change scheme. Then, we revised the dependency of soil decomposition rates on soil temperature and moisture. We further refined the cold-season methane processes by updating upper boundary resistance that allows  $\text{CH}_4$  to be emitted from frozen soils through snow to  
 530 the atmosphere. We also used the updated ELMV1-ECA to estimate historical trends of cold-season  $\text{CH}_4$  and  $\text{CO}_2$  net emissions at the Alaskan tundra sites from 1950 to 2017. This study is among the first efforts toward improving simulations of zero-curtain periods and cold-season carbon emissions over Arctic tundra by ESMs. The strategy of improving ELMV1-ECA phase-change scheme and environmental controls on microbial activity can be easily applied to other global land models.

535

With the revised phase-change scheme, the updated ELMv1-ECA greatly improved site-scale simulations of soil temperature, soil moisture, and zero-curtain period. Specifically, the RMSE of daily subsurface soil temperature was substantially reduced compared to the baseline simulation, showing site-averaged improvements ranging from 58% to 87% over the early cold season (Sep. to Oct.) and from 36% to 46% over the annual cycle for soil layers within the active layer.

540 The evaluation of simulated liquid water content with the new phase-change scheme, although limited by availability of observations, showed a relative reduction in RMSE as high as 43% for the 5<sup>th</sup> layer at ATQ, and site-averaged improvements of 15% and 21% for the 4<sup>th</sup> and 5<sup>th</sup> layer, respectively. Simulated ZCP durations were also greatly improved, with, e.g.,



relative reductions in MAEs of 65%, 65%, 66%, and 50% for the 4<sup>th</sup> layer (about 12 cm) at BES/CMDL, BEO, ATQ, and IVO, respectively.

545

Based upon the improved simulations of soil temperature and moisture with the new phase-change scheme, the identified an optimal SOC decomposition scheme, and the revised methane module, the site-averaged mean annual errors of cold-season emissions were reduced by 84% and 81% for CH<sub>4</sub> and CO<sub>2</sub>, respectively. We also found that CH<sub>4</sub> and CO<sub>2</sub> emissions over the early cold season, i.e., September and October, which usually accounts for most of the zero-curtain period, contributed more than 50% of the total emissions throughout the cold season (September to May). Zero-curtain period durations showed increasing trends from 1950 to 2017, with larger trends in deeper soil layers. Although the annual CO<sub>2</sub> emissions did not show statistically significant trends, both CO<sub>2</sub> emissions during the 12 cm depth zero-curtain period and the entire cold-season period (Sep. to May) showed increasing trends.

555 Although showing improvements compared to baseline results, the new simulations generally overestimated the contribution of early cold season CO<sub>2</sub> emissions. Many reasons could contribute to the overestimations, including poor representation of coupled biogeochemical and hydrological processes in the localized permafrost soil environment, the lack of accurate representation of inundated hydro-ecological dynamics, underestimation of snow accumulation due to micro-topographic effects and thus the snow insulation to the ground (e.g., Bisht et al., 2018), among others. Strong microtopographic impacts on CO<sub>2</sub> and CH<sub>4</sub> emissions across seven landscape types in Barrow, Alaska, were recently reported (Wang et al. (2019); Grant et al., 2017a; Grant et al., 2017b). In addition, the single static multiplicative function ( $f_{total} = f_T f_W f_O f_D$ ) used to parameterize the total impact of environmental conditions on respiration might not be appropriate (Tang and Riley, 2019). Also, inappropriately prescribed land cover at the site scale or inaccurate climate forcing (particularly air temperature and precipitation; Chang et al. (2019)) could all impact snow accumulation processes (Tao et al., 2017), which can significantly impact CO<sub>2</sub> and CH<sub>4</sub> emission simulations. Customizing the complex local ecosystem vegetation community might be feasible at the site scale, however, it is less possible for regional or global land model simulations. This issue calls for the importance of upscaling methods to model (e.g., Pau et al., 2016; Liu et al., 2016) and measure (e.g., Natali et al., 2019; Virkkala et al., 2019) carbon and water cycle dynamics at the regional and global scales.

570 Given the persistent warming and the continued more severe warming in the cold season (Box et al., 2019), we envision continuing increases in cold-season CO<sub>2</sub> and CH<sub>4</sub> emissions from the permafrost tundra ecosystem. The increasing rate of cold-season heterotrophic respiration (releasing CO<sub>2</sub>) may become larger than the trend of warm-season vegetation CO<sub>2</sub> uptake under future climate. To accurately characterize cold-season emissions and warm-season net uptake, models have to correctly simulate both components, which, however, few models can do. The updated ELMv1-ECA, with the enhanced capacity to reproduce cold-season CO<sub>2</sub> and CH<sub>4</sub> emissions proven by this study, can serve as a starting point to better predict permafrost carbon responses to future climate. Finally, the complex water-carbon interactions require modelling systems



with fully coupled hydrological-thermal-biogeochemical processes to better predict the carbon budget in permafrost regions under future climate.

#### **Code/Data availability**

580 The observations used in this study are available at <http://dx.doi.org/10.3334/ornldaac/1300> and <https://doi.org/10.3334/ornldaac/1562>. The UAF observations are available at <http://permafrost.gi.alaska.edu>. The updated version of ELMv1-ECA will be available at GitHub.

#### **Author contributions**

585 JT assembled observations, developed the methodology, conducted model simulations, analysed results, and wrote and revised the paper. QZ contributed to experiment design, editing the original and revised manuscript. WJR and RBN edited the original and revised manuscript, and provided valuable discussion and guidance.

#### **Competing interests**

The authors declare that they have no conflict of interest.

#### **Acknowledgments**

590 We are grateful for valuable discussions with Jinyun Tang, Roisin Commane, Xiyan Xu, Kai Yang, and Chenghai Wang. We thank the anonymous reviewers for their helpful comments. This material is based upon work supported by the U.S. Department of Energy, Office of Science, Office of Biological and Environmental Research under Award Number DE-SC0019063.

#### **Appendices: Description of Relevant Modules within ELMv1-ECA**

595 Here we describe the heat transfer in subsurface soils, the carbon decomposition, and the methane module within the ELMv1-ECA that are of particular relevance to our study.

#### **Appendix A Subsurface Heat Transfer**

ELMv1-ECA approximates the subsurface heat transfer process with a one-dimensional heat diffusion equation:



$$c \frac{\partial T}{\partial t} = \frac{\partial}{\partial z} \left( \lambda \frac{\partial T}{\partial z} \right), \quad (\text{Eq. A1})$$

where  $T$  is the soil temperature (K),  $c$  is the volumetric soil heat capacity ( $\text{J m}^{-3} \text{K}^{-1}$ ),  $\lambda$  is soil thermal conductivity ( $\text{W m}^{-1} \text{K}^{-1}$ ), and  $z$  is the soil depth (m) of the ELMv1-ECA soil layers. The ELMv1-ECA soil column consists of 15 layers, with soil thickness increasing exponentially with depth. The bottom of soil column is down to 42 m, and the top 10 layers are hydrologically active with layer node depth as 0.0071 m, 0.0279 m, 0.0623 m, 0.1189 m, 0.2122 m, 0.3661 m, 0.6198 m, 1.0380 m, 1.7276 m, 2.8646 m, respectively. The soil heat capacity and thermal conductivity is updated at each time step based on the fractions of soil matrix components, i.e., liquid water content, ice content, and soil solids. The impact of organic carbon on soil thermal and hydraulic properties was incorporated as a linear combination of the counterparts properties of mineral soil and organic matter (Lawrence and Slater, 2008). To solve the (Eq. A1), ELMv1-ECA employs the Crank-Nicholson method, resulting in a tridiagonal system equation. We assume a zero-flux bottom boundary condition. The top boundary condition is estimated by solving the energy balance equation at the air and ground interface, with additionally an overlying five-layer snow model and a one-layer surface water model in between. When snow and surface water present, ELMv1-ECA incorporates the snow layers and surface water layer into the tridiagonal system to solve the heat transfer along the entire column.

ELMv1-ECA incorporates freeze-thaw processes of soil water in a decoupled way. Specifically, the model determines the onset of melting or freezing by soil temperature initially solved at time step  $n + 1$  without consideration of the phase change process, denoted as  $T_i^{n+1}$ , i.e.,

$$\begin{aligned} T_i^{n+1} > T_f \text{ and } w_{ice,i}^n > 0 & \quad \text{melting} \\ T_i^{n+1} < T_f \text{ and } w_{liq,i}^n > w_{liq,max,i}^{n+1} & \quad \text{freezing} \end{aligned}, \quad (\text{Eq. A2})$$

where  $T_f$  is the freezing temperature of water ( $0^\circ\text{C}$  in Kelvin, i.e., 273.15 K),  $w_{ice,i}^n$  and  $w_{liq,i}^n$  is the mass of ice and liquid water ( $\text{kg m}^{-2}$ ) of layer  $i$ , and  $w_{liq,max,i}^{n+1}$  ( $\text{kg m}^{-2}$ ) is the supercooled liquid water that is allowed to coexist with ice given the subfreezing soil temperature  $T_i^{n+1}$ . This  $w_{liq,max,i}^{n+1}$  varies with soil texture and temperature and is calculated by the freezing point depression equation (Niu and Yang, 2006),

$$w_{liq,max,i}^{n+1} = \Delta z_i \theta_{sat,i} \left[ \frac{10^3 L_f (T_f - T_i^{n+1})}{g T_i^{n+1} \psi_{sat,i}} \right]^{-1/B_i}, \quad (\text{Eq. A3})$$

where  $\Delta z_i$  is the soil thickness of the  $i$ th layer (in mm),  $\theta_{sat,i}$  represents the soil porosity (i.e., the saturated volumetric water content),  $L_f$  is the latent heat of fusion ( $\text{J kg}^{-1}$ ),  $B_i$  is the Clapp and Hornberger exponent (Clapp and Hornberger, 1978),  $g$  is the gravitational acceleration ( $\text{m s}^{-2}$ ), and  $\psi_{sat,i}$  is the soil texture-dependent saturated matric potential (mm).



The rate of phase change is initially assessed from the heat excess (or deficit) needed to change the estimated temperature to the freezing point. Specifically, the model first computes the energy ( $H_i$ ) needed for adjusting current soil temperature ( $T_i^{n+1}$ ) to  $T_f$ :

$$\begin{aligned} H_i &= -c_i \frac{\Delta z_i}{\Delta t} T_{inc} + (1 - f_{sno} - f_{h2osfc}) \frac{\partial h}{\partial T} T_{inc} & i = 1 \\ H_i &= -c_i \frac{\Delta z_i}{\Delta t} T_{inc} & i > 1 \end{aligned} \quad (\text{Eq. A4})$$

where  $T_{inc} = T_f - T_i^{n+1}$ ,  $h$  is ground heat flux,  $f_{sno}$  and  $f_{h2osfc}$  is the snow and surface water fraction within the grid cell, respectively. The mass change involved then is computed as  $H_m = \frac{H_i \Delta t}{L_f}$  (i.e.,  $-c_i \frac{\Delta z_i}{L_f} T_{inc}$  for soils below the top interface layer). That is, the mass of ice increased/decreased by freezing/melting is  $-H_m$ , releasing/absorbing energy  $H_i$  to bring up/down the current soil temperature to  $T_f$ . Accordingly, the ice and liquid mass are adjusted as:

$$\begin{aligned} w_{ice,i}^{n+1} &= \begin{cases} \min(w_{ice,i}^n + w_{liq,i}^n - w_{liq,max,i}^{n+1}, w_{ice,i}^n - H_m) & w_{liq,i}^n + w_{ice,i}^n \geq w_{liq,max,i}^{n+1} \\ 0 & w_{liq,i}^n + w_{ice,i}^n < w_{liq,max,i}^{n+1} \end{cases} \\ w_{liq,i}^{n+1} &= \max(w_{liq,i}^n + w_{ice,i}^n - w_{ice,i}^{n+1}, 0) \end{aligned} \quad (\text{Eq. A5})$$

The  $H_i$  then is adjusted to  $H_i^*$ , calculated as  $H_i^* = H_i - \frac{L_f(w_{ice,i}^n - w_{ice,i}^{n+1})}{\Delta t}$ . The  $H_i^*$  then is the ultimately determined latent heat and is used to further readjust soil temperature as in equation (Eq. A6),

$$T_i^{n+1*} = T_f + \frac{\Delta t}{c_i \Delta z_i} H_i^* = T_f - \frac{L_f(w_{ice,i}^n - w_{ice,i}^{n+1})}{c_i \Delta z_i}, \quad (\text{Eq. A6})$$

in which the temperature adjusted to  $T_f$  is further increased by  $-\frac{L_f(w_{ice,i}^n - w_{ice,i}^{n+1})}{c_i \Delta z_i}$  due to soil freezing since  $w_{ice,i}^{n+1} \geq w_{ice,i}^n$ , or decreased due to melting when  $w_{ice,i}^{n+1} < w_{ice,i}^n$ .

We revised the phase-change scheme mainly through incorporating a phase-change efficiency ( $\varepsilon$ ) and replacing the constant freezing point  $T_f$  with the temperature of the freezing point depression in (Eq. A2). The phase-change efficiency, introduced by Le Moigne et al. (2012) and adopted by Masson et al. (2013) and Yang et al. (2018a), is calculated as,

$$\begin{cases} \varepsilon_{liq,i}^n = \frac{\theta_{liq,i}^n}{\theta_{sat,i}^n} & \text{for freezing} \\ \varepsilon_{ice,i}^n = \frac{\theta_{ice,i}^n}{\theta_{sat,i}^n} & \text{for melting} \end{cases}, \quad (\text{Eq. A7})$$

where  $\theta_{liq,i}^n$  and  $\theta_{ice,i}^n$  is the soil liquid and ice volumetric water content of layer  $i$  at previous time step  $n$ , respectively, and  $\theta_{sat,i}$  represents the soil porosity (i.e., the saturated volumetric water content).



The temperature of the freezing point depression, as a virtual temperature ( $T_v$ ) reversely derived from the freezing point temperature-depression equation, i.e.,  $\psi(T) = \frac{L_f(T_f - T_i)}{10^3 T}$  (Fuchs et al., 1978; Cary and Mayland, 1972), is calculated as,

$$T_v^{n+1*} = \frac{10^3 L_f T_f}{10^3 L_f + g \psi_i^n}, \quad (\text{Eq. A8})$$

where  $L_f$  is the latent heat of fusion ( $\text{J kg}^{-1}$ ) and  $g$  is the gravitational acceleration ( $\text{m s}^{-2}$ ).  $\psi_i^n$  is the soil water potential (mm), calculated as the soil water retention curve of Clapp and Hornberger (1978), i.e.,  $\psi_i^n = \psi_{sat,i} \left( \frac{\theta_{liq,i}^n}{\theta_{sat,i}} \right)^{-B_i}$ , where  $\theta_{liq,i}^n = w_{liq,i}^n / \Delta z_i$  as in (Eq. A3),  $B_i$  is the Clapp and Hornberger exponent, and  $\psi_{sat,i}$  is the soil texture-dependent saturated matric potential (mm).

## Appendix B Decomposition Cascade Model

Within the ELMv1-ECA Century decomposition cascade model, the respiration fractions are parameterized as the fraction of the decomposition carbon flux out of each carbon pool, including litter and soil organic matter. The base decomposition rate is modified by a function representing environmental controls on soil decomposition which accounts for the impacts of individual factors including temperature ( $f_T$ ) and moisture ( $f_W$ ), an oxygen scalar ( $f_O$ ), and a depth scalar ( $f_D$ ), in a multiplicative way, i.e.,  $f_{total} = f_T f_W f_O f_D$ .

We use a  $Q_{10}$ -based standard exponential function to account for the temperature effect on decomposition,

$$f_T = Q_{10}^{\left( \frac{T - T_{ref}}{10} \right)}, \quad (\text{Eq. B9})$$

where  $Q_{10} = 1.5$  on default, which is consistent with ecosystem-level observations (Mahecha et al., 2010), and  $T_{ref}$  is the reference temperature ( $25^\circ\text{C}$ ). During cold seasons when soil temperature becomes subfreezing, respiration continues but with more controls from liquid water stress. The original moisture scalar ( $f_W$ ) within ELMV1-ECA is given in the formulation, calculated as,

$$f_W = \begin{cases} 0 & \text{For } \psi_i < \psi_{min} \\ \frac{\log(\psi_{min}/\psi_i)}{\log(\psi_{min}/\psi_{max})} & \text{For } \psi_{min} \leq \psi_i \leq \psi_{max} \\ 1 & \text{For } \psi_i > \psi_{max} \end{cases}, \quad (\text{Eq. B10})$$

where  $\psi_i = \psi_{max} \left( \frac{\theta_{liq,i}}{\theta_{sat,i}} \right)^{-B_i}$  is the soil water potential, where  $B_i$  is the Clapp and Hornberger exponent (Clapp and Hornberger, 1978). In frozen soil, the soil water potential is related to soil temperature through the freezing point depression



equation, i.e.,  $\psi_i = \frac{L_f(T_f - T_i)}{10^3 T}$  (Fuchs et al., 1978; Cary and Mayland, 1972) in the supercooled water formulation (Niu and Yang, 2006). Thus, the liquid water stress on decomposition is translated into dependency on temperature when soil temperature is below the freezing point.

ELMv1-ECA approximates oxygen stress ( $f_o$ ) as the ratio of available oxygen to that demanded by decomposers, and has a minimum value of 0.2 (Oleson et al., 2013). As described by section 3.1.2, we now incorporate the oxygen stress into the moisture scalar. The revised moisture scalar  $f_w^*$  is calculated as below,

$$f_w^* = \begin{cases} \max \left[ \frac{\log \left( \frac{\psi_{min}}{\psi_{max} S_{fliq} - B_i} \right)}{\log \left( \frac{\psi_{min}}{\psi_{max}} \right)}, f_{w\_min} \right] & \text{For } S_{fliq} < S_{fop} \\ \max \left[ \frac{\log \left( \frac{\psi_{min}}{\psi_{max} S_{fliq} - B_i} \right)}{\log \left( \frac{\psi_{min}}{\psi_{max}} \right)} \times \left( \frac{1 - S_{fliq}}{1 - S_{fop}} \right)^b, f_{w\_min} \right] & \text{For } S_{fliq} \geq S_{fop} \end{cases}, \quad (\text{Eq. B11})$$

where  $S_{fliq}$  is the degree of saturation, calculated as the ratio of soil volumetric liquid water content to porosity (i.e.,  $\frac{\theta_{liq,i}}{\theta_{sat,i}}$ ),  $S_{fop}$  is an optimal threshold beyond which the decomposition will be suppressed by oxygen stress, and  $b$  is a parameter controlling the shape of the decreasing limb, and  $f_{w\_min}$  is a minimum threshold for  $f_w^*$ .

The depth scalar ( $f_D = \exp \left( -\frac{z_i}{Z_\tau} \right)$ ) represents unresolved other depth-dependent processes (e.g., soil microbial dynamics, priming effects, etc.) (Koven et al., 2013b; Lawrence et al., 2015; Koven et al., 2015). Applying the depth scalar to decomposition rates would exponentially decrease the respiration fluxes along with the vertical soil layers. The  $Z_\tau$  is the e-folding depth for decomposition, and by default  $Z_\tau$  is 0.5 m (Oleson et al., 2013).

### Appendix C Methane Model

The ELMv1-ECA methane model includes the representations of  $\text{CH}_4$  production, oxidation, and three pathways of transport (i.e., aerenchyma tissues, ebullition, aqueous and gaseous diffusion), and solves the transient reaction diffusion equation for  $\text{CH}_4$ . ELMv1-ECA estimates  $\text{CH}_4$  production ( $P$ ;  $\text{mol m}^{-3} \text{s}^{-1}$ ) in the anaerobic portion of the soil column based on the upland heterotrophic respiration ( $HR$ ;  $\text{mol C m}^{-2} \text{s}^{-1}$ ) from soil and litter, further adjusted by factors representing influence from soil temperature ( $f_T$ ), pH ( $f_{pH}$ ), redox potential ( $f_{pE}$ ), and seasonal inundation condition ( $S$ ) (Riley et al., 2011), expressed as,

$$P = HR \times f_{CH_4} \times f_T \times f_{pH} \times f_{pE} \times S. \quad (\text{Eq. C12})$$



The  $f_{CH_4}$  is a fraction of anaerobically mineralized carbon atoms becoming  $CH_4$ . Detailed explanation on other factors can be found in (Riley et al., 2011). The methane production  $P$  will be directly impacted by the changes to water and heat transfer (Appendix A) and HR (Appendix B). The ultimately estimated  $CH_4$  emissions are also controlled by oxidation, transport mechanisms (i.e., aerenchyma transport, ebullition, and diffusion), and the upper boundary resistance. Detailed descriptions on  $CH_4$  oxidation and transport mechanisms are provided in (Riley et al., 2011). Here we modified  $CH_4$  transport mechanisms for facilitating reasonable cold-season  $CH_4$  emissions.

Vascular plants aerenchyma tissues serve as diffusive pathways for  $CH_4$  to transport from soil layer  $z$  ( $A(z)$ ,  $\text{mol m}^{-2} \text{s}^{-1}$ ) to the atmosphere, calculated as:

$$A(z) = (C(z) - C_a) / \left( \frac{r_L z}{D p T_{aere} \rho_r(z)} + r_a \right) \quad , \quad (\text{Eq. C13})$$

where  $C(z)$  and  $C_a$  is the gaseous  $CH_4$  concentration ( $\text{mol m}^{-3}$ ) in soil depth  $z$  and in the atmosphere, respectively;  $r_a$  is the aerodynamic resistance ( $\text{s m}^{-1}$ );  $D$  is the gas diffusion coefficient ( $\text{m}^2 \text{s}^{-1}$ );  $p$  is aerenchyma porosity (-);  $r_L$  is the ratio of root length to vertical depth (i.e., root obliquity); and  $\rho_r(z)$  is the root fraction in soil depth  $z$  (-).  $T_{aere}$  is the specific aerenchyma area ( $\text{m}^2 \text{m}^{-2}$ ), and is expressed as,

$$T_{aere} = \frac{f_N N_a LAI}{0.22} \pi R^2, \quad (\text{Eq. C14})$$

where  $R$  represents the aerenchyma radius ( $=2.9 \times 10^{-3} \text{ m}$ );  $N_a$  is the annual net primary production (NPP), and  $f_N$  is the belowground fraction of current NPP; and the factor 0.22 is the amount of carbon per tiller. We integrate the emissions from ice cracks and remnants of aerenchyma tissues with (Eq. C14) by removing temperature limitation and applying a small  $T_{aere}$  during winter time, where  $T_{aere}$  now represents areas adding up ice crack fractions and remnants of aerenchyma tissues.

ELMv1-ECA estimates aqueous diffusion below water table as,

$$D_e = \begin{cases} D_0 \theta_{sat}^2 & \text{For } T \geq 0^\circ\text{C} \\ D_0 \theta_{sat}^2 f_{frzsoil} & \text{For } T < 0^\circ\text{C} \end{cases} \quad (\text{Eq. C15})$$

where  $D_0$  is the diffusion coefficient ( $\text{m}^2 \text{s}^{-1}$ ),  $\theta_{sat}$  is the soil porosity,  $f_{frzsoil}$  is a scaling factor for frozen soils, defined as  $f_{frzsoil} = \frac{V_{liq}}{V_{liq} + V_{ice}}$  where  $V_{liq}$  and  $V_{ice}$  is the volume ( $\text{m}^3 \text{m}^{-3}$ ) of liquid water and ice, respectively. In subfreezing soils when  $T < 0^\circ$ ,  $D_e$  is largely limited by liquid water content. Upon sensitivity experiments, we alleviated this limitation by assuming a half deduction for the diffusion coefficient in saturated, frozen soils, i.e.,  $f_{frzsoil} = 0.5$ . We also decreased snow resistance by introducing new scale factors (Table 2) which intend to increase the conductance at the upper boundary when snow presents.





## References

- Anthony, K. M. W., Anthony, P., Grosse, G., and Chanton, J.: Geologic methane seeps along boundaries of Arctic  
 715 permafrost thaw and melting glaciers, *Nat Geosci*, 5, 419-426, 2012.
- Arndt, K. A., Oechel, W. C., Goodrich, J. P., Bailey, B. A., Kalhori, A., Hashemi, J., Sweeney, C., and Zona, D.: Sensitivity  
 of Methane Emissions to Later Soil Freezing in Arctic Tundra Ecosystems, *J Geophys Res-Bioge*, 124, 2595-2609,  
 10.1029/2019JG005242, 2019.
- Belshe, E. F., Schuur, E. A. G., and Bolker, B. M.: Tundra ecosystems observed to be CO<sub>2</sub> sources due to differential  
 720 amplification of the carbon cycle, *Ecol Lett*, 16, 1307-1315, 10.1111/ele.12164, 2013.
- Bhanja, S. N., and Wang, J. Y.: Estimating influences of environmental drivers on soil heterotrophic respiration in the  
 Athabasca River Basin, Canada, *Environ Pollut*, 257, 2020.
- Bisht, G., Riley, W. J., Wainwright, H. M., Dafflon, B., Yuan, F. M., and Romanovsky, V. E.: Impacts of microtopographic  
 snow redistribution and lateral subsurface processes on hydrologic and thermal states in an Arctic polygonal ground  
 725 ecosystem: a case study using ELM-3D v1.0, *Geosci Model Dev*, 11, 61-76, 2018.
- Box, J. E., Colgan, W. T., Christensen, T. R., Schmidt, N. M., Lund, M., Parmentier, F. J. W., Brown, R., Bhatt, U. S.,  
 Euskirchen, E. S., Romanovsky, V. E., Walsh, J. E., Overland, J. E., Wang, M. Y., Corell, R. W., Meier, W. N.,  
 Wouters, B., Mernild, S., Mard, J., Pawlak, J., and Olsen, M. S.: Key indicators of Arctic climate change: 1971-2017,  
*Environmental Research Letters*, 14, 2019.
- 730 Cary, J. W., and Mayland, H. F.: Salt and Water Movement in Unsaturated Frozen Soil, *Soil Sci Soc Am Pro*, 36, 549-&,  
 1972.
- Chang, K. Y., Riley, W. J., Crill, P. M., Grant, R. F., Rich, V. I., and Saleska, S. R.: Large carbon cycle sensitivities to  
 climate across a permafrost thaw gradient in subarctic Sweden, *Cryosphere*, 13, 647-663, 2019.
- Clapp, R. B., and Hornberger, G. M.: Empirical equations for some soil hydraulic properties, *Water Resources Research*, 14,  
 735 601-604, 1978.
- Commane, R., Lindaas, J., Benmergui, J., Luus, K. A., Chang, R. Y. W., Daube, B. C., Euskirchen, E. S., Henderson, J. M.,  
 Karion, A., Miller, J. B., Miller, S. M., Parazoo, N. C., Randerson, J. T., Sweeney, C., Tans, P., Thoning, K.,  
 Veraverbeke, S., Miller, C. E., and Wofsy, S. C.: Carbon dioxide sources from Alaska driven by increasing early winter  
 respiration from Arctic tundra, *P Natl Acad Sci USA*, 114, 5361-5366, 2017.
- 740 Dankers, R., Burke, E. J., and Price, J.: Simulation of permafrost and seasonal thaw depth in the JULES land surface scheme,  
*Cryosphere*, 5, 773-790, 2011.
- Davidson, E. A., and Janssens, I. A.: Temperature sensitivity of soil carbon decomposition and feedbacks to climate change,  
*Nature*, 440, 165-173, 2006.
- Davidson, S. J., and Zona, D.: Arctic Vegetation Plots in Flux Tower Footprints, North Slope, Alaska, 2014, ORNL DAAC,  
 745 Oak Ridge, Tennessee, USA. <https://doi.org/10.3334/ORNLDAAAC/1546>, 2018.



- Etiopio, G., and Klusman, R. W.: Microseepage in drylands: Flux and implications in the global atmospheric source/sink budget of methane, *Global and Planetary Change*, 72, 265-274, 2010.
- Fahnestock, J. T., Jones, M. H., Brooks, P. D., Walker, D. A., and Welker, J. M.: Winter and early spring CO<sub>2</sub> efflux from tundra communities of northern Alaska, *Journal of Geophysical Research-Atmospheres*, 103, 29023-29027, Doi 10.1029/98jd00805, 1998.
- Fuchs, M., Campbell, G., and Papendick, R.: An analysis of sensible and latent heat flow in a partially frozen unsaturated soil, *Soil Sci Soc Am J*, 42, 379-385, 1978.
- Golaz, J. C., Caldwell, P. M., Van Roekel, L. P., Petersen, M. R., Tang, Q., Wolfe, J. D., Abeshu, G., Anantharaj, V., Asay-Davis, X. S., Bader, D. C., Baldwin, S. A., Bisht, G., Bogenschütz, P. A., Branstetter, M., Brunke, M. A., Brus, S. R., Burrows, S. M., Cameron-Smith, P. J., Donahue, A. S., Deakin, M., Easter, R. C., Evans, K. J., Feng, Y., Flanner, M., Foucar, J. G., Fyke, J. G., Griffin, B. M., Hannay, C., Harrop, B. E., Hoffman, M. J., Hunke, E. C., Jacob, R. L., Jacobsen, D. W., Jeffery, N., Jones, P. W., Keen, N. D., Klein, S. A., Larson, V. E., Leung, L. R., Li, H. Y., Lin, W. Y., Lipscomb, W. H., Ma, P. L., Mahajan, S., Maltrud, M. E., Mametjanov, A., McClean, J. L., McCoy, R. B., Neale, R. B., Price, S. F., Qian, Y., Rasch, P. J., Eyre, J. E. J. R., Riley, W. J., Ringler, T. D., Roberts, A. F., Roesler, E. L., Salinger, A. G., Shaheen, Z., Shi, X. Y., Singh, B., Tang, J. Y., Taylor, M. A., Thornton, P. E., Turner, A. K., Veneziani, M., Wan, H., Wang, H. L., Wang, S. L., Williams, D. N., Wolfram, P. J., Worley, P. H., Xie, S. C., Yang, Y., Yoon, J. H., Zelinka, M. D., Zender, C. S., Zeng, X. B., Zhang, C. Z., Zhang, K., Zhang, Y., Zheng, X., Zhou, T., and Zhu, Q.: The DOE E3SM Coupled Model Version 1: Overview and Evaluation at Standard Resolution, *J Adv Model Earth Sy*, 11, 2089-2129, 2019.
- Graf, A., Weihermüller, L., Huisman, J. A., Herbst, M., and Vereecken, H.: Comment on "Global Convergence in the Temperature Sensitivity of Respiration at Ecosystem Level", *Science*, 331, 1265-+, 2011.
- Grant, R. F., Mekonnen, Z. A., Riley, W. J., Arora, B., and Torn, M. S.: Mathematical Modelling of Arctic Polygonal Tundra with Ecosys: 2. Microtopography Determines How CO<sub>2</sub> and CH<sub>4</sub> Exchange Responds to Changes in Temperature and Precipitation, *J Geophys Res-Bioge*, 122, 3174-3187, 2017a.
- Grant, R. F., Mekonnen, Z. A., Riley, W. J., Wainwright, H. M., Graham, D., and Torn, M. S.: Mathematical Modelling of Arctic Polygonal Tundra with Ecosys: 1. Microtopography Determines How Active Layer Depths Respond to Changes in Temperature and Precipitation, *J Geophys Res-Bioge*, 122, 3161-3173, 2017b.
- Harris, I.: CRU JRA v1. 1: A forcings dataset of gridded land surface blend of Climatic Research Unit (CRU) and Japanese reanalysis (JRA) data; Jan. 1901-Dec. 2017. Published by: University of East Anglia Climatic Research Unit, Centre for Environmental Data Analysis, 2905 doi: 10.5285/13f3635174794bb98cf8ac4b0ee8f4ed, 2019.
- Jones, M. H., Fahnestock, J. T., and Welker, J. M.: Early and late winter CO<sub>2</sub> efflux from arctic tundra in the Kuparuk River watershed, Alaska, USA, *Arct Antarct Alp Res*, 31, 187-190, Doi 10.2307/1552607, 1999.
- Kim, D., Lee, M. I., and Seo, E.: Improvement of Soil Respiration Parameterization in a Dynamic Global Vegetation Model and Its Impact on the Simulation of Terrestrial Carbon Fluxes, *Journal of Climate*, 32, 127-143, 2019.



- 780 Kim, Y., Ueyama, M., Nakagawa, F., Tsunogai, U., Harazono, Y., and Tanaka, N.: Assessment of winter fluxes of CO<sub>2</sub> and  
CH<sub>4</sub> in boreal forest soils of central Alaska estimated by the profile method and the chamber method: a diagnosis of  
methane emission and implications for the regional carbon budget, *Tellus B: Chemical and Physical Meteorology*, 59,  
223-233, 2007.
- Kittler, F., Heimann, M., Kolle, O., Zimov, N., Zimov, S., and Gockede, M.: Long-Term Drainage Reduces CO<sub>2</sub> Uptake and  
785 CH<sub>4</sub> Emissions in a Siberian Permafrost Ecosystem, *Global Biogeochemical Cycles*, 31, 1704-1717, 2017.
- Koven, C. D., Ringeval, B., Friedlingstein, P., Ciais, P., Cadule, P., Khvorostyanov, D., Krinner, G., and Tarnocai, C.:  
Permafrost carbon-climate feedbacks accelerate global warming, *P Natl Acad Sci USA*, 108, 14769-14774, 2011.
- Koven, C. D., Riley, W. J., and Stern, A.: Analysis of Permafrost Thermal Dynamics and Response to Climate Change in the  
CMIP5 Earth System Models, *Journal of Climate*, 26, 1877-1900, 10.1175/Jcli-D-12-00228.1, 2013a.
- 790 Koven, C. D., Riley, W. J., Subin, Z. M., Tang, J. Y., Torn, M. S., Collins, W. D., Bonan, G. B., Lawrence, D. M., and  
Swenson, S. C.: The effect of vertically resolved soil biogeochemistry and alternate soil C and N models on C dynamics  
of CLM4, *Biogeosciences*, 10, 7109-7131, 2013b.
- Koven, C. D., Lawrence, D. M., and Riley, W. J.: Permafrost carbon-climate feedback is sensitive to deep soil carbon  
decomposability but not deep soil nitrogen dynamics, *P Natl Acad Sci USA*, 112, 3752-3757,  
795 10.1073/pnas.1415123112, 2015.
- Koven, C. D., Hugelius, G., Lawrence, D. M., and Wieder, W. R.: Higher climatological temperature sensitivity of soil  
carbon in cold than warm climates, *Nat Clim Change*, 7, 817-+, 10.1038/Nclimate3421, 2017.
- Kurylyk, B. L., and Hayashi, M.: Improved Stefan Equation Correction Factors to Accommodate Sensible Heat Storage  
during Soil Freezing or Thawing, *Permafrost Periglac*, 27, 189-203, 2016.
- 800 Lawrence, D. M., and Slater, A. G.: Incorporating organic soil into a global climate model, *Clim Dynam*, 30, 145-160,  
10.1007/s00382-007-0278-1, 2008.
- Lawrence, D. M., Koven, C. D., Swenson, S. C., Riley, W. J., and Slater, A. G.: Permafrost thaw and resulting soil moisture  
changes regulate projected high-latitude CO<sub>2</sub> and CH<sub>4</sub> emissions, *Environmental Research Letters*, 10, 10.1088/1748-  
9326/10/9/094011, 2015.
- 805 Le Moigne, P., Boone, A., Belamari, S., Brun, E., Calvet, J., Decharme, B., Faroux, S., Gibelin, A., Giordani, H., Lafont, S.,  
Lebeaupin, C., Le Moigne, P., Mahfouf, J., Martin, E., Masson, V., Mironov, D., Morin, S., Noilhan, J., Tulet, P., Van  
den Hurk, B., and Vionnet, V.: SURFEX Scientific Documentation, Note de centre (CNRM/GMME), Météo-France,  
Toulouse, France, 2012.
- Liu, Y. N., Bisht, G., Subin, Z. M., Riley, W. J., and Pau, G. S. H.: A Hybrid Reduced-Order Model of Fine-Resolution  
810 Hydrologic Simulations at a Polygonal Tundra Site, *Vadose Zone J*, 15, 2016.
- Lyman, S. N., Tran, H. N., Mansfield, M. L., Bowers, R., and Smith, A.: Strong temporal variability in methane fluxes from  
natural gas well pad soils, *Atmospheric Pollution Research*, 2020.



- Mahecha, M. D., Reichstein, M., Carvalhais, N., Lasslop, G., Lange, H., Seneviratne, S. I., Vargas, R., Ammann, C., Arain,  
 M. A., Cescatti, A., Janssens, I. A., Migliavacca, M., Montagnani, L., and Richardson, A. D.: Global Convergence in the  
 815 Temperature Sensitivity of Respiration at Ecosystem Level, *Science*, 329, 838-840, 2010.
- Masson, V., Le Moigne, P., Martin, E., Faroux, S., Alias, A., Alkama, R., Belamari, S., Barbu, A., Boone, A., Bouysse, F.,  
 Brousseau, P., Brun, E., Calvet, J. C., Carrer, D., Decharme, B., Delire, C., Donier, S., Essauini, K., Gibelin, A. L.,  
 Giordani, H., Habets, F., Jidane, M., Kerdraon, G., Kourzeneva, E., Lafaysse, M., Lafont, S., Brossier, C. L., Lemonsu,  
 A., Mahfouf, J. F., Marguinaud, P., Mokhtari, M., Morin, S., Pigeon, G., Salgado, R., Seity, Y., Taillefer, F., Tanguy,  
 820 G., Tulet, P., Vincendon, B., Vionnet, V., and Voldoire, A.: The SURFEXv7.2 land and ocean surface platform for  
 coupled or offline simulation of earth surface variables and fluxes, *Geosci Model Dev*, 6, 929-960, 2013.
- Mekonnen, Z. A., Riley, W. J., Grant, R. F., and Romanovsky, V.: Changes in precipitation and air temperature contribute  
 comparably to permafrost degradation in a warmer climate, *Environ Res Lett*, 2020.
- Meyer, N., Welp, G., and Amelung, W.: The Temperature Sensitivity (Q<sub>10</sub>) of Soil Respiration: Controlling Factors and  
 825 Spatial Prediction at Regional Scale Based on Environmental Soil Classes, *Global Biogeochemical Cycles*, 32, 306-323,  
 2018.
- Moriasi, D. N., Arnold, J. G., Van Liew, M. W., Bingner, R. L., Harmel, R. D., and Veith, T. L.: Model evaluation  
 guidelines for systematic quantification of accuracy in watershed simulations, *Transactions of the Asabe*, 50, 885-900,  
 2007.
- 830 Moyano, F. E., Manzoni, S., and Chenu, C.: Responses of soil heterotrophic respiration to moisture availability: An  
 exploration of processes and models, *Soil Biol Biochem*, 59, 72-85, 2013.
- Nash, J. E., and Sutcliffe, J. V.: River flow forecasting through conceptual models part I — A discussion of principles, *J.*  
*Hydrol.*, 10, 282-290, 10.1016/0022-1694(70)90255-6, 1970.
- Natali, S. M., Watts, J. D., Rogers, B. M., Potter, S., Ludwig, S. M., Selbmann, A.-K., Sullivan, P. F., Abbott, B. W., Arndt,  
 835 K. A., Birch, L., Björkman, M. P., Bloom, A. A., Celis, G., Christensen, T. R., Christiansen, C. T., Commane, R.,  
 Cooper, E. J., Crill, P., Czimczik, C., Davydov, S., Du, J., Egan, J. E., Elberling, B., Euskirchen, E. S., Friborg, T.,  
 Genet, H., Göckede, M., Goodrich, J. P., Grogan, P., Helbig, M., Jafarov, E. E., Jastrow, J. D., Kalhori, A. A. M., Kim,  
 Y., Kimball, J. S., Kutzbach, L., Lara, M. J., Larsen, K. S., Lee, B.-Y., Liu, Z., Lorant, M. M., Lund, M., Lupascu, M.,  
 Madani, N., Malhotra, A., Matamala, R., McFarland, J., McGuire, A. D., Michelsen, A., Minions, C., Oechel, W. C.,  
 840 Olefeldt, D., Parmentier, F.-J. W., Pirk, N., Poulter, B., Quinton, W., Rezanezhad, F., Risk, D., Sachs, T., Schaefer, K.,  
 Schmidt, N. M., Schuur, E. A. G., Semenchuk, P. R., Shaver, G., Sonnentag, O., Starr, G., Treat, C. C., Waldrop, M. P.,  
 Wang, Y., Welker, J., Wille, C., Xu, X., Zhang, Z., Zhuang, Q., and Zona, D.: Large loss of CO<sub>2</sub> in winter observed  
 across the northern permafrost region, *Nat Clim Change*, 10.1038/s41558-019-0592-8, 2019.
- Neumann, R. B., Moorberg, C. J., Lundquist, J. D., Turner, J. C., Waldrop, M. P., McFarland, J. W., Euskirchen, E. S.,  
 845 Edgar, C. W., and Turetsky, M. R.: Warming effects of spring rainfall increase methane emissions from thawing  
 permafrost, *Geophys Res Lett*, 2019.



- Nicolisky, D. J., Romanovsky, V. E., Alexeev, V. A., and Lawrence, D. M.: Improved modeling of permafrost dynamics in a GCM land-surface scheme, *Geophys Res Lett*, 34, 2007.
- Niu, G. Y., and Yang, Z. L.: Effects of frozen soil on snowmelt runoff and soil water storage at a continental scale, *J. Hydrometeorol.*, 7, 937-952, 2006.
- Oechel, W. C., Vourlitis, G. L., Hastings, S. J., Zulueta, R. C., Hinzman, L., and Kane, D.: Acclimation of ecosystem CO<sub>2</sub> exchange in the Alaskan Arctic in response to decadal climate warming, *Nature*, 406, 978-981, 2000.
- Oechel, W. C., Laskowski, C. A., Burba, G., Gioli, B., and Kalhori, A. A. M.: Annual patterns and budget of CO<sub>2</sub> flux in an Arctic tussock tundra ecosystem, *J Geophys Res-Bioge*, 119, 323-339, 2014.
- 855 Oechel, W. C., and Kalhori, A.: ABoVE: CO<sub>2</sub> and CH<sub>4</sub> Fluxes and Meteorology at Flux Tower Sites, Alaska, 2015-2017, <https://doi.org/10.3334/ornl-daac/1562>, 2018.
- Oleson, K. W., Lawrence, D., Bonan, G., Drewniak, B., Huang, M., Koven, C., Levis, S., Li, F., Riley, W., and Subin, Z.: Technical Description of version 4.5 of the Community Land Model (CLM)(NCAR Technical Note No. NCAR/TN-503+STR). Citeseer, National Center for Atmospheric Research, PO Box, 3000, 2013.
- 860 Outcalt, S. I., Nelson, F. E., and Hinkel, K. M.: The Zero-Curtain Effect - Heat and Mass-Transfer across an Isothermal Region in Freezing Soil, *Water Resources Research*, 26, 1509-1516, 1990.
- Pau, G. S. H., Shen, C. P., Riley, W. J., and Liu, Y. N.: Accurate and efficient prediction of fine-resolution hydrologic and carbon dynamic simulations from coarse-resolution models, *Water Resources Research*, 52, 791-812, 2016.
- Piao, S. L., Ciais, P., Friedlingstein, P., Peylin, P., Reichstein, M., Luysaert, S., Margolis, H., Fang, J. Y., Barr, A., Chen, A.
- 865 P., Grelle, A., Hollinger, D. Y., Laurila, T., Lindroth, A., Richardson, A. D., and Vesala, T.: Net carbon dioxide losses of northern ecosystems in response to autumn warming, *Nature*, 451, 49-U43, 2008.
- Rafique, R., Xia, J. Y., Hararuk, O., Asrar, G. R., Leng, G. Y., Wang, Y. P., and Luo, Y. Q.: Divergent predictions of carbon storage between two global land models: attribution of the causes through traceability analysis, *Earth Syst Dynam*, 7, 2016.
- 870 Riley, W. J., Subin, Z. M., Lawrence, D. M., Swenson, S. C., Torn, M. S., Meng, L., Mahowald, N. M., and Hess, P.: Barriers to predicting changes in global terrestrial methane fluxes: analyses using CLM4Me, a methane biogeochemistry model integrated in CESM, *Biogeosciences*, 8, 1925-1953, 10.5194/bg-8-1925-2011, 2011.
- Romanovsky, V. E., Kholodov, A. L., Cable, W. L., Cohen, L., Panda, S., Marchenko, S., Muskett, R. R., and Nicolisky, D.: Network of Permafrost Observatories in North America and Russia, 10.18739/A2SH27, 2009.
- 875 Russell, S. J., Bohrer, G., Johnson, D. R., Villa, J. A., Heltzel, R., Rey-Sanchez, C., and Matthes, J. H.: Quantifying CH<sub>4</sub> concentration spikes above baseline and attributing CH<sub>4</sub> sources to hydraulic fracturing activities by continuous monitoring at an off-site tower, *Atmos Environ*, 117452, 2020.
- Sapriza-Azuri, G., Gamazo, P., Razavi, S., and Wheeler, H. S.: On the appropriate definition of soil profile configuration and initial conditions for land surface-hydrology models in cold regions, *Hydrol Earth Syst Sc*, 22, 3295-3309, 10.5194/hess-22-3295-2018, 2018.
- 880



- Sierra, C. A., Trumbore, S. E., Davidson, E. A., Vicca, S., and Janssens, I.: Sensitivity of decomposition rates of soil organic matter with respect to simultaneous changes in temperature and moisture, *J Adv Model Earth Sy*, 7, 335-356, 2015.
- Sierra, C. A., Malghani, S., and Loescher, H. W.: Interactions among temperature, moisture, and oxygen concentrations in controlling decomposition rates in a boreal forest soil, *Biogeosciences*, 14, 703-710, 2017.
- 885 Tang, J. Y., and Riley, W. J.: Weaker soil carbon-climate feedbacks resulting from microbial and abiotic interactions, *Nat Clim Change*, 5, 56-60, 10.1038/Nclimate2438, 2015.
- Tang, J. Y., and Riley, W. J.: A Theory of Effective Microbial Substrate Affinity Parameters in Variably Saturated Soils and an Example Application to Aerobic Soil Heterotrophic Respiration, *J Geophys Res-Bioge*, 124, 918-940, 2019.
- Tao, J., Reichle, R. H., Koster, R. D., Forman, B. A., and Xue, Y.: Evaluation and Enhancement of Permafrost Modeling  
890 With the NASA Catchment Land Surface Model, *J Adv Model Earth Sy*, 9, 2771-2795, 2017.
- Tao, J., Koster, R. D., Reichle, R. H., Forman, B. A., Xue, Y., Chen, R. H., and Moghaddam, M.: Permafrost variability over the Northern Hemisphere based on the MERRA-2 reanalysis, *The Cryosphere*, 13, 2087-2110, 2019.
- Taylor, M. A., Celis, G., Ledman, J. D., Bracho, R., and Schuur, E. A. G.: Methane Efflux Measured by Eddy Covariance in Alaskan Upland Tundra Undergoing Permafrost Degradation, *J Geophys Res-Bioge*, 123, 2695-2710, 2018.
- 895 Virkkala, A.-M., Aalto, J. A., Tagesson, T., Treat, C. C., Lehtonen, A., Rogers, B. M., Natali, S., and Luoto, M.: High-latitude terrestrial regions remain a CO<sub>2</sub> sink over 1990-2015, *AGUFM*, 2019, B43E-01, 2019.
- Wang, Y. H., Yuan, F. M., Yuan, F. H., Gu, B. H., Hahn, M. S., Torn, M. S., Ricciuto, D. M., Kumar, J., He, L. Y., Zona, D., Lipson, D. A., Wagner, R., Oechel, W. C., Wullschlegel, S. D., Thornton, P. E., and Xu, X. F.: Mechanistic Modeling of Microtopographic Impacts on CO<sub>2</sub> and CH<sub>4</sub> Fluxes in an Alaskan Tundra Ecosystem Using the CLM-  
900 Microbe Model, *J Adv Model Earth Sy*, 11, 4288-4304, 2019.
- Wilkman, E., Zona, D., Tang, Y. F., Gioli, B., Lipson, D. A., and Oechel, W.: Temperature Response of Respiration Across the Heterogeneous Landscape of the Alaskan Arctic Tundra, *J Geophys Res-Bioge*, 123, 2287-2302, 2018.
- Xu, X. Y., Riley, W. J., Koven, C. D., Billesbach, D. P., Chang, R. Y. W., Commene, R., Euskirchen, E. S., Hartery, S., Harazono, Y., Iwata, H., McDonald, K. C., Miller, C. E., Oechel, W. C., Poulter, B., Raz-Yaseef, N., Sweeney, C., Torn,  
905 M., Wofsy, S. C., Zhang, Z., and Zona, D.: A multi-scale comparison of modeled and observed seasonal methane emissions in northern wetlands, *Biogeosciences*, 13, 5043-5056, 10.5194/bg-13-5043-2016, 2016.
- Yan, Z. F., Bond-Lamberty, B., Todd-Brown, K. E., Bailey, V. L., Li, S. L., Liu, C. Q., and Liu, C. X.: A moisture function of soil heterotrophic respiration that incorporates microscale processes, *Nat Commun*, 9, 2018.
- Yang, K., Wang, C. H., and Li, S. Y.: Improved Simulation of Frozen-Thawing Process in Land Surface Model (CLM4.5),  
910 *Journal of Geophysical Research-Atmospheres*, 123, 13238-13258, 2018a.
- Yang, Q., Dan, L., Wu, J., Jiang, R., Dan, J., Li, W., Yang, F., Yang, X., and Xia, L.: The Improved Freeze-Thaw Process of a Climate-Vegetation Model: Calibration and Validation Tests in the Source Region of the Yellow River, *Journal of Geophysical Research-Atmospheres*, 123, 13346-13367, 2018b.



- Zhou, T., Shi, P. J., Hui, D. F., and Luo, Y. Q.: Global pattern of temperature sensitivity of soil heterotrophic respiration  
915 (Q(10)) and its implications for carbon-climate feedback, *J Geophys Res-Bioge*, 114, 2009.
- Zhu, Q., Riley, W. J., Tang, J. Y., Collier, N., Hoffman, F. M., Yang, X. J., and Bisht, G.: Representing Nitrogen, Phosphorus, and Carbon Interactions in the E3SM Land Model: Development and Global Benchmarking, *J Adv Model Earth Sy*, 11, 2238-2258, 2019.
- Zona, D., Gioli, B., Commane, R., Lindaas, J., Wofsy, S. C., Miller, C. E., Dinardo, S. J., Dengel, S., Sweeney, C., and  
920 Karion, A.: Cold season emissions dominate the Arctic tundra methane budget, *Proceedings of the National Academy of Sciences*, 113, 40-45, 2016.



**Table 1: Specific modifications made to ELMv1-ECA. Process interactions are illustrated in Figure 2.**

	<b>Part 1 – Phase-change scheme within the heat transfer module</b>		<b>Part 2 – Environmental modifier to the base decomposition rate</b>		<b>Part 3 – Methane module</b>	
Relevant processes influenced	Water and heat transfer, plant and soil respiration, plant productivity, CO <sub>2</sub> fluxes and CH <sub>4</sub> emissions.		Plant and soil respiration, plant productivity, CO <sub>2</sub> fluxes and CH <sub>4</sub> emissions.		CH <sub>4</sub> emissions	
	Original	New	Original	New	Original	New
Variables or equations influenced	Eq. A2-6	Imposing Eq. A7 and Eq. A8 to Eq. A2-A6	Eq. B9-B10	Eq. B11 and changes in Table S2	Eq. C13-C15	1. Applying a minimum LAI to (Eq. C14) to mimic ice cracks and remnants of aerenchyma tissues in frozen soils, and permitting transport even when temperature is below 0°C. 2. Introducing new scale factors for snow resistance: $\text{scale\_factor\_gasdiff\_snow} = \text{scale\_factor\_gasdiff} * 100$ $\text{scale\_factor\_liqdiff\_snow} = \text{scale\_factor\_liqdiff} * 100$ 3. Introducing a new scale factor for diffusivity in frozen soil: $f_{frzsoil} = 0.5$ in (Eq. C15)

925





**Table 2: List of Designed Site-Scale Experiments. Process interactions among the three parts are illustrated in Figure 2.**

Experiment Name	Part 1 - Phase Change Scheme within Heat Transfer Model		Part 2 – Environmental Modifier within Carbon Decomposition Model		Part 3 – Methane Model	
	Original	New	Original	New	Original	New
OriPC_OriDecom_OriCH4 (Baseline)	√		√		√	
NewPC_OriDecom_OriCH4		√	√		√	
NewPC_OriDecom_NewCH4		√	√			√
NewPC_NewDecom_NewCH4*						
(NewPC_OptimalDecom_NewCH4) <sup>#</sup>		√		√		√
(NewPC_GenericDecom_NewCH4) <sup>\$</sup>						

930 \*Replacing the original temperature- and moisture-dependency functions on decomposition rates with 200 new functions of environmental modifiers as listed in Table S2 in the supplementary file.

# “NewPC\_OptimalDecom\_NewCH4” is the optimal simulation among the 200 “NewPC\_NewDecom\_NewCH4” cases at each site.

\$“NewPC\_GenericDecom\_NewCH4” means the simulation with the identified generic scheme that can be applied to regional simulation. The generic scheme is the common satisfactory scheme that provides the best overall performance for all the sites.

935



**Table 3: Mean absolute error (MAE) of simulated ZCP (days) with the original phase-change scheme (Ori\_PC) and newly resized phase-change scheme (NewPC), and the relative improvement (%) of using the new phase-change scheme compared to the baseline results, calculated as  $100\% \times (\text{MAE\_ZCP\_OriPC} - \text{MAE\_ZCP\_NewPC}) / \text{MAE\_ZCP\_OriPC}$ .**

	BES&CMDL			BEO			ATQ			IVO		
	MAE_ZCP_OriPC (days)	MAE_ZCP_NewPC (days)	Improvement (%)	MAE_ZCP_OriPC (days)	MAE_ZCP_NewPC (days)	Improvement (%)	MAE_ZCP_OriPC (days)	MAE_ZCP_NewPC (days)	Improvement (%)	MAE_ZCP_OriPC (days)	MAE_ZCP_NewPC (days)	Improvement (%)
<b>Layer 1</b>	38.80	31.40	19.07	37.60	33.20	11.70	26.33	13.33	49.37	54.00	51.50	4.63
<b>Layer 2</b>	29.20	14.20	51.37	27.40	12.60	54.01	24.33	5.67	76.71	50.50	37.50	25.74
<b>Layer 3</b>	35.20	18.40	47.73	33.60	16.80	50.00	28.00	9.33	66.67	55.75	30.25	45.74
<b>Layer 4</b>	29.60	10.40	64.86	30.60	10.60	65.36	28.67	9.67	66.28	61.50	30.50	50.41
<b>Layer 5</b>	18.00	11.40	36.67	17.60	10.80	38.64	27.67	17.33	37.35	54.50	22.00	59.63
<b>Layer 6</b>	77.40	12.20	84.24	77.40	13.00	83.20	61.67	36.67	40.54	68.00	14.75	78.31
<b>Layer 7</b>	NaN	NaN	NaN	NaN	NaN	NaN	NaN	NaN	NaN	151.33	46.67	69.16

940



**Table 4: RMSE (°C) of simulated soil temperatures with the original phase-change (PC) scheme and newly resized PC scheme. NaN represents the cases when observations are not available.**

Model Layer (Node Depth)	BES&CMDL		BEO		ATQ		IVO	
	Ori_PC	New_PC	Ori_PC	New_PC	Ori_PC	New_PC	Ori_PC	New_PC
Layer 1 (0.01 m)	5.66	3.82	5.45	3.85	6.47	3.77	9.12	5.42
Layer 2 (0.03 m)	5.36	3.35	5.16	3.45	6.42	3.66	9.08	5.22
Layer 3 (0.06 m)	5.32	3.16	5.16	3.28	6.38	3.54	8.87	4.91
Layer 4 (0.12 m)	5.25	2.92	5.22	3.00	6.33	3.40	8.87	4.81
Layer 5 (0.21 m)	5.15	2.72	4.90	2.82	6.24	3.32	8.76	4.60
Layer 6 (0.37 m)	4.70	2.56	4.70	2.56	6.15	3.50	8.67	4.42
Layer 7 (0.62 m)	4.41	2.33	4.41	2.34	NaN	NaN	8.38	4.08
Layer 8 (1.04 m)	4.23	2.13	4.22	2.14	NaN	NaN	7.75	3.46
Layer 9 (1.73 m)	4.33	2.04	4.32	2.07	NaN	NaN	NaN	NaN
Layer 10 (2.86 m)	4.28	2.19	4.27	2.22	NaN	NaN	NaN	NaN
Layer 11 (4.74 m)	3.96	2.11	3.96	2.13	NaN	NaN	NaN	NaN
Layer 12 (7.83 m)	2.92	1.51	2.92	1.52	NaN	NaN	NaN	NaN
Layer 13 (12.93 m)	2.77	0.74	2.78	0.78	NaN	NaN	NaN	NaN
Layer 14 (21.33 m)	NaN	NaN	NaN	NaN	NaN	NaN	NaN	NaN
Layer 15 (35.18 m)	NaN	NaN	NaN	NaN	NaN	NaN	NaN	NaN



**Table 5: Total CH<sub>4</sub> emissions and CO<sub>2</sub> net flux over three seasonal periods, including the early cold season, cold season, and the warm season. The “ELM\_New” here means NewPC\_OptimalDecom\_NewCH<sub>4</sub> (Table 2). The percentage of each seasonal total CH<sub>4</sub> emissions to the annual total is included in the brackets.**

Total CH <sub>4</sub> Emissions (gC m <sup>-2</sup> )	BES/CMDL			BEO			ATQ		
	Early Cold Season (Sep. and Oct.)	Cold Season (Sep. to May)	Warm Season (Jun. to Aug.)	Early Cold Season (Sep. and Oct.)	Cold Season (Sep. to May)	Warm Season (Jun. to Aug.)	Early Cold Season (Sep. and Oct.)	Cold Season (Sep. to May)	Warm Season (Jun. to Aug.)
<b>ELM_Baseline</b>	0.08 (4.7%)	0.08 (5.1%)	1.53 (94.9%)	0.09 (5.5%)	0.10 (6.2%)	1.54 (93.8%)	0.16 (15.1%)	0.16 (15.3%)	0.89 (84.7%)
<b>ELM_New</b>	0.73 (23.3%)	1.19 (37.9%)	1.95 (62.1%)	0.77 (21.7%)	1.46 (41.4%)	2.07 (58.6%)	0.31 (17.6%)	0.51 (28.3%)	1.23 (70.7%)
<b>Observation</b>	0.63 (21.0%)	1.32 (44.5%)	1.65 (55.5%)	0.83 (24.4%)	1.43 (41.9%)	1.97 (58.1%)	0.36 (19.2%)	0.85 (44.7%)	1.04 (55.3%)
Total CO <sub>2</sub> Net Flux (gC m <sup>-2</sup> )	BES/CMDL			BEO			ATQ		
	Early Cold Season (Sep. and Oct.)	Cold Season (Sep. to May)	Warm Season (Jun. to Aug.)	Early Cold Season (Sep. and Oct.)	Cold Season (Sep. to May)	Warm Season (Jun. to Aug.)	Early Cold Season (Sep. and Oct.)	Cold Season (Sep. to May)	Warm Season (Jun. to Aug.)
<b>ELM_Baseline</b>	31.27	31.38	2.03	30.99	31.14	13.91	40.46	40.86	-26.05
<b>ELM_New</b>	48.50	89.94	-61.87	49.10	97.65	-55.47	59.14	82.55	-46.64
<b>Observation</b>	43.60	87.50	-67.61	28.20	96.14	-64.33	24.29	58.64	-62.41

950



**Table 6: Historical trend of ZCP durations (days year<sup>-1</sup>) for each soil layer from 1950 to 2017. (Trends with  $p > 0.05$  are not statistically significant.)**

	BES/CMDL		BEO		ATQ	
	Trend (days yr <sup>-1</sup> )	p Value	Trend (days yr <sup>-1</sup> )	p Value	Trend (days yr <sup>-1</sup> )	p Value
ZCP Duration of Layer 1	-0.02	0.73	-0.02	0.73	0.07	0.40
ZCP Duration of Layer 2	0.09	0.03	0.09	0.04	0.14	0.05
ZCP Duration of Layer 3	0.10	0.03	0.12	0.01	0.15	0.05
ZCP Duration of Layer 4	0.10	0.07	0.10	0.09	0.21	0.01
ZCP Duration of Layer 5	0.11	0.10	0.11	0.09	0.23	0.02
ZCP Duration of Layer 6	0.37	0.51	0.35	0.56	0.49	0.00



Table 7: Historical trend (1950 - 2017) in site-scale heterotrophic respiration, CH<sub>4</sub> emission, and CO<sub>2</sub> flux during the ZCP duration at 12 cm (4<sup>th</sup> layer), cold-season months (Sep. - May), and the whole annual cycle (Sep. - Aug.). (Trends with  $p > 0.05$  are not statistically significant.)

Not statistically significant.)

	BES/CMDL		BEO		ATQ	
	Trend of Heterotrophic Respiration					
	Trend (g C m <sup>-2</sup> yr <sup>-1</sup> )	p Value	Trend (g C m <sup>-2</sup> yr <sup>-1</sup> )	p Value	Trend (g C m <sup>-2</sup> yr <sup>-1</sup> )	p Value
ZCP duration at 12 cm	0.02	0.17	0.02	0.24	0.07	0.00
Cold Season (Sep.-May)	0.09	0.00	0.09	0.00	0.13	0.00
Annual (Sep.-Aug.)	0.21	0.00	0.18	0.00	0.30	0.00
	Trend of CH <sub>4</sub> Emission					
	Trend (mg C m <sup>-2</sup> yr <sup>-1</sup> )	p Value	Trend (mg C m <sup>-2</sup> yr <sup>-1</sup> )	p Value	Trend (mg C m <sup>-2</sup> yr <sup>-1</sup> )	p Value
ZCP duration at 12 cm	-7.61	0.01	-7.89	0.00	-0.66	0.73
Cold Season (Sep.-May)	-2.54	0.22	-3.19	0.13	2.50	0.13
Annual (Sep.-Aug.)	-4.98	0.20	-5.63	0.15	10.56	0.00
	Trend of CO <sub>2</sub> Net Emissions					
	Trend (g C m <sup>-2</sup> yr <sup>-1</sup> )	p Value	Trend (g C m <sup>-2</sup> yr <sup>-1</sup> )	p Value	Trend (g C m <sup>-2</sup> yr <sup>-1</sup> )	p Value
ZCP duration at 12 cm	0.20	0.00	0.19	0.00	0.26	0.00
Cold Season (Sep.-May)	0.36	0.00	0.33	0.00	0.38	0.00
Annual (Sep.-Aug.)	0.08	0.68	0.10	0.64	0.18	0.47

960

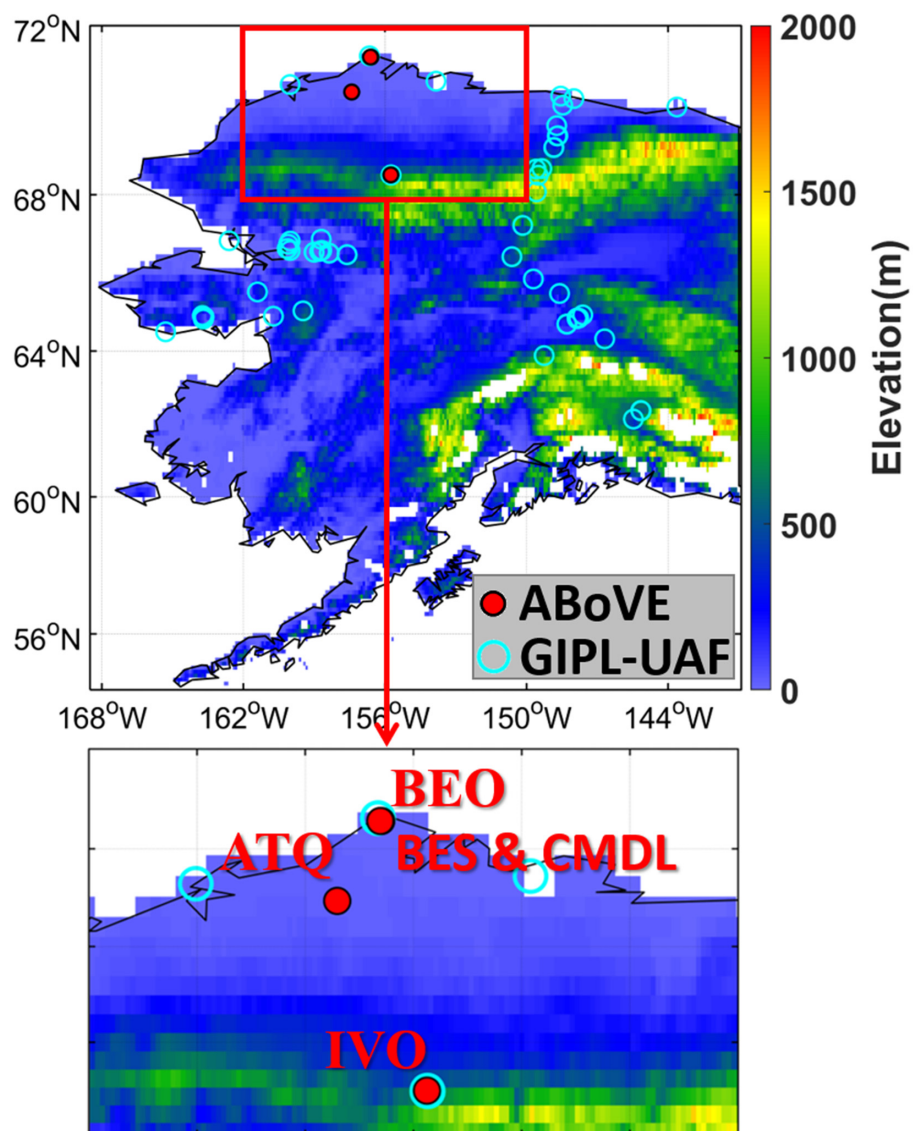


Figure 1: Red dots indicate the five ABoVE flux tower sites used in this study. Cyan circles are GIPL-UAF permafrost sites.

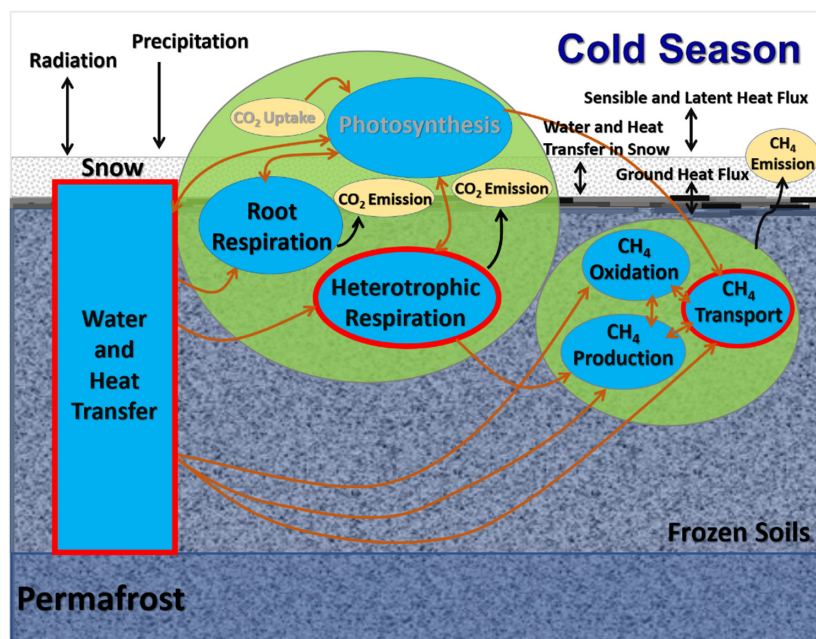


Figure 2: Schematic diagram illustrating the interactions between the water and heat transfer module, vegetation and carbon decomposition module, and the methane module within the ELMv1-ECA over the tundra ecosystem during the cold season. Some other important processes but not discussed this study, including nutrient dynamics, oxygen reaction and diffusion, etc., are not illustrated here. Grey colours indicate processes that are not actively involved during the cold season over the tundra ecosystem. Orange arrows represent process interactions. Black arrows represent fluxes. Ellipses with thicker red boundaries indicate the modules we modified. Specifically, we revised the new soil water phase-change scheme within the water and heat transfer module, modified carbon decomposition environmental scalar scheme, and incorporated the modified CH<sub>4</sub> transport mechanism for the cold-season regime.



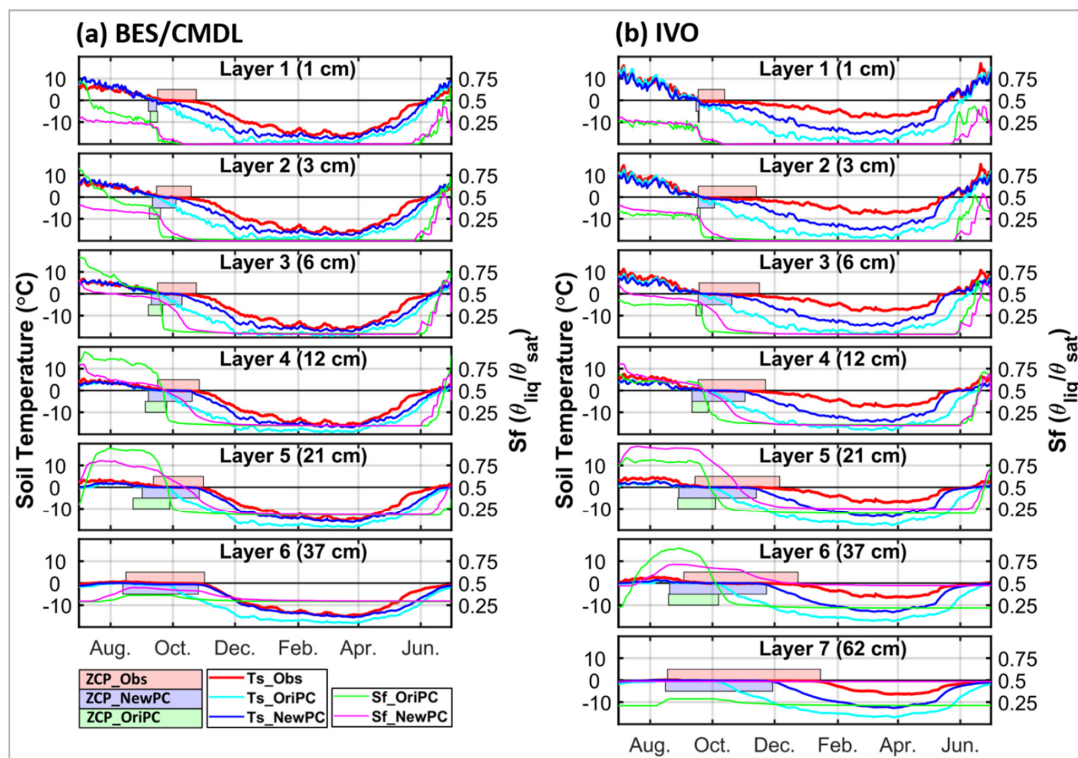


Figure 3: Comparison of multi-year (2013 - 2017) averaged daily soil temperatures observed ( $T_{s\_Obs}$ , red) and simulated with the original ( $T_{s\_OriPC}$ , cyan) and improved ( $T_{s\_NewPC}$ , blue) phase-change schemes at BES/CMDL (a) and IVO (b). Simulated moisture saturation with the original ( $Sf\_OriPC$ ; green) and improved ( $Sf\_NewPC$ ; magenta) schemes are shown on the right hand axes. The horizontal axes indicates days from July to June, with ticks represent the first day of each month. Hatched areas represent durations of zero-curtain periods observed ( $ZCP\_Obs$ , orange) and simulated ( $ZCP\_OriPC$ , green;  $ZCP\_NewPC$ , blue). No baseline ZCP is shown in the 6<sup>th</sup> layer for BES/CMDL and the 7<sup>th</sup> layer for IVO because the maximum annual temperature is below 0°C.

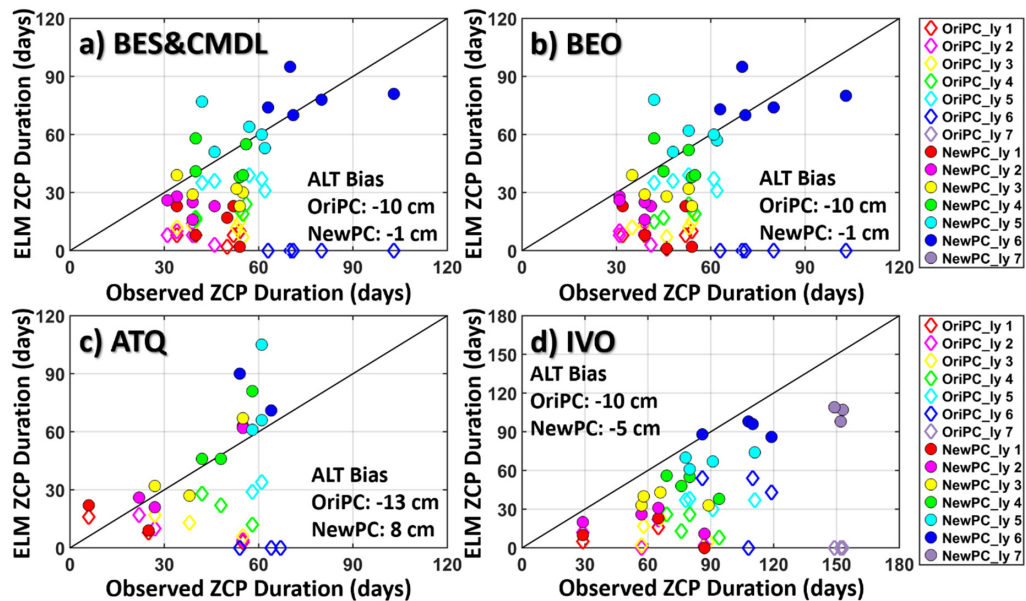
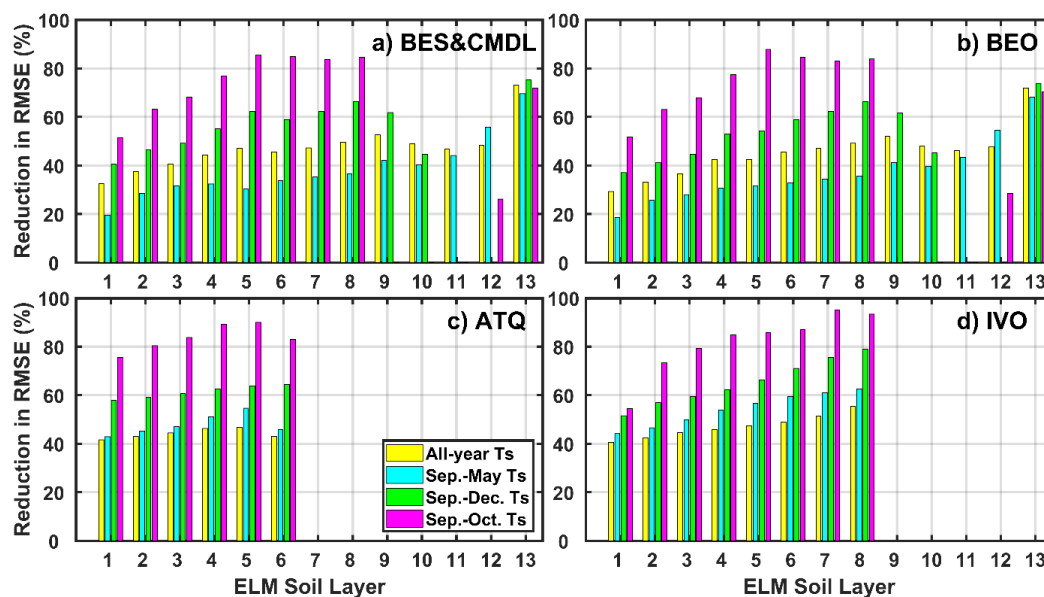


Figure 4: Comparison between observed and ELMv1-ECA simulated durations of ZCP for the original (OriPC; open diamonds) and improved (NewPC; solid circles) phase-change schemes over four annual cycles (July to June) from 2013 to 2017. “ly” means model layer. Simulated ZCP durations with NewPC demonstrate significant improvements compared to OriPC (solid dots vs. open diamonds), especially for the 4<sup>th</sup> to the deepest layer above permafrost. Note, a zero days ZCP means that the maximum daily temperature during an annual cycle is below 0°C. The pairs of zero vs. non-zero days ZCP (e.g., OriPC\_ly 7 at IVO and OriPC\_ly 6 at other sites) indicate that baseline results underestimated ALT. The bias (simulation - observation) of multi-year averaged ALT simulated by the two experiments is provided in each panel.



995 Figure 5: Relative improvement in the RMSE of simulated soil temperature with the new phase-change scheme (RMSE\_Ts\_NewPC) compared to that with the original scheme (RMSE\_Ts\_OriPC), calculated as  $100\% \times (\text{RMSE\_Ts\_OriPC} - \text{RMSE\_Ts\_NewPC}) / \text{RMSE\_Ts\_OriPC}$ .

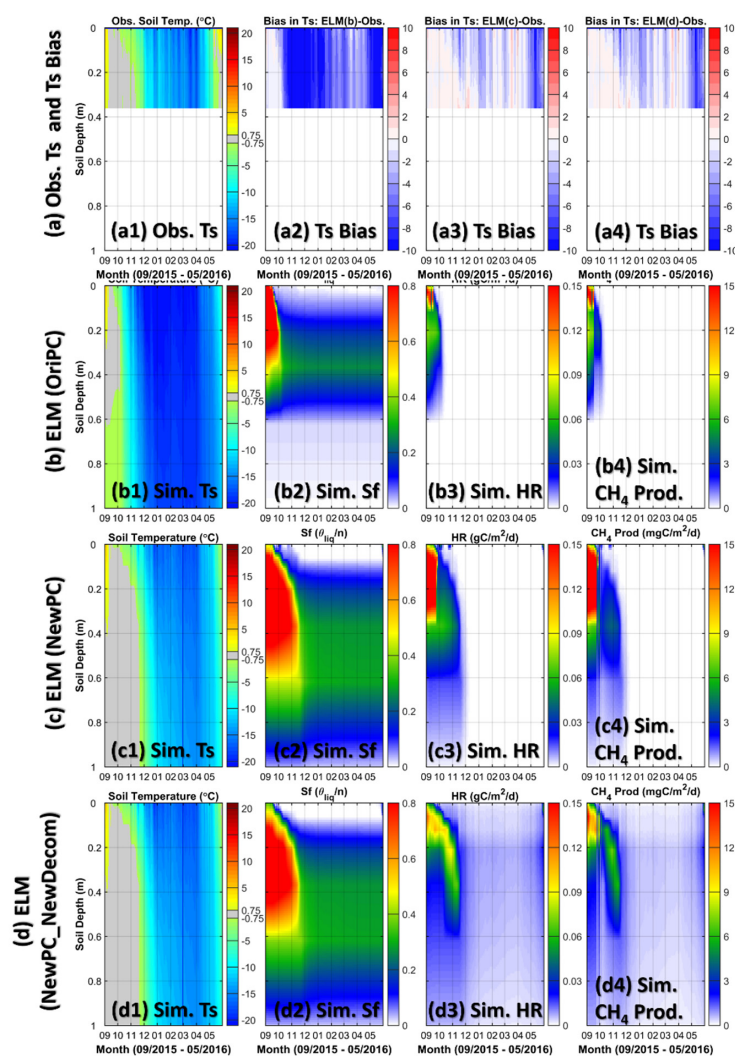


Figure 6: (a1) Observed temporal evolution of vertical profiles of soil temperature at ATQ over the cold season from Sep. 1, 2015 to May 31, 2016, and the biases of soil temperatures from three simulations (a2, a3, a4). ELMv1-ECA simulated baseline evolution of soil temperature (b1), soil liquid water content (b2), heterotrophic respiration, and CH<sub>4</sub> production. (c) Same as (b) with the new phase-change scheme (i.e., NewPC\_OriDecom\_OriCH<sub>4</sub>). (d) Same as (c), but using the revised ELMV1-ECA soil moisture-dependency function scheme-2 with built-in oxygen stress (see Figure S1), i.e., NewPC\_NewDecom\_OriCH<sub>4</sub>. Soil temperatures within the range of  $[-0.75^\circ, 0.75^\circ]$  are coloured by grey, indicating a two-dimensional “zero-curtain zone”.

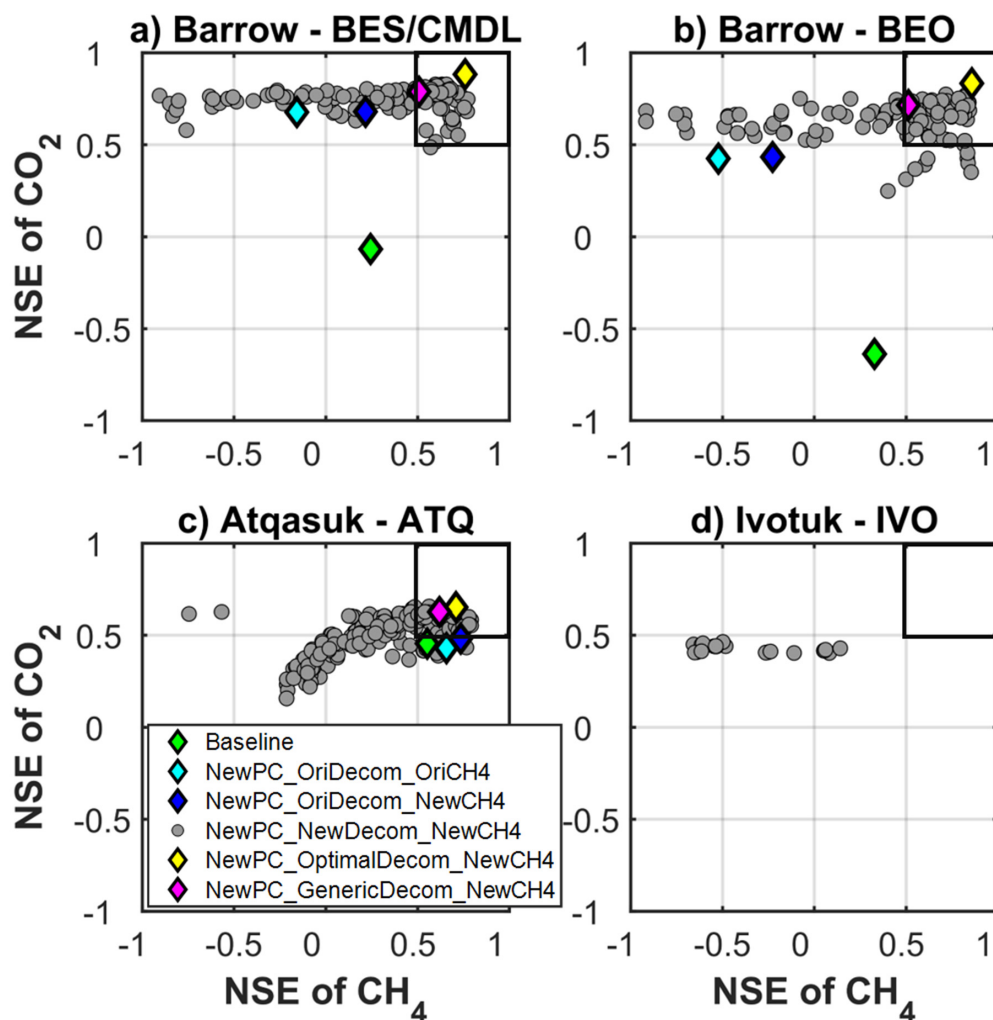
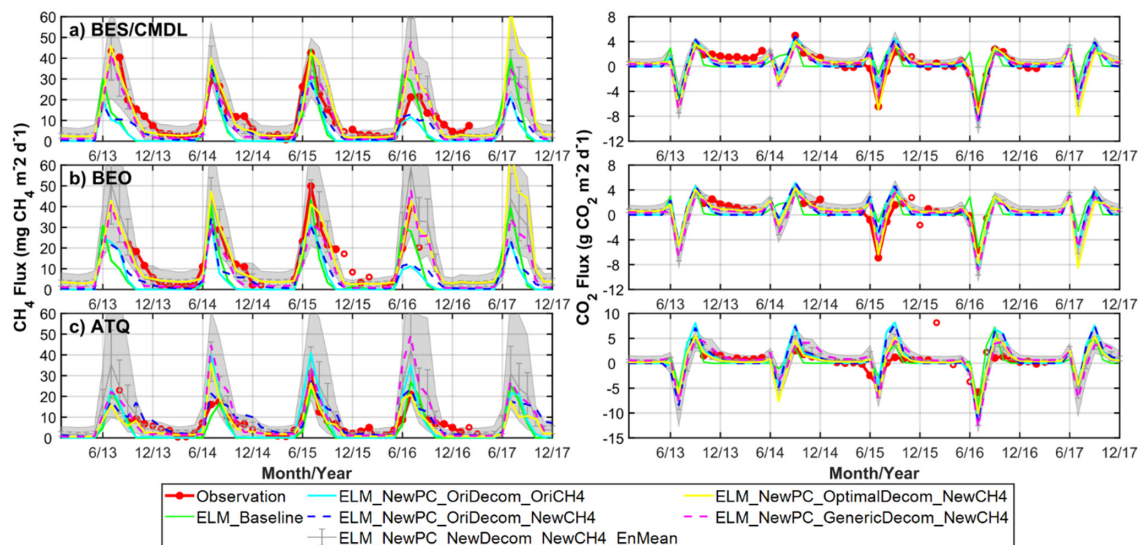


Figure 7: Scatter plot between the Nash–Sutcliffe Efficiency (NSE) of simulated monthly  $\text{CH}_4$  and  $\text{CO}_2$  emissions. An ideal simulation has both NSEs of  $\text{CH}_4$  and  $\text{CO}_2$  as one (i.e., the upper right corner). The boxes encompass simulations with satisfactory performance (NSE > 0.5). Optimal (yellow) – the best simulation for each site; Generic (magenta) – the simulation with a common decomposition scheme that provides best overall performance for all the sites. See Table 2 for the configuration for each experiment. Symbols outside the plotting ranges indicate poor performance, e.g., (-34.9, -0.3) for baseline at IVO, thus are be shown in the figure.



**Figure 8:** Observed and simulated monthly  $\text{CH}_4$  (left) and  $\text{CO}_2$  (right) net flux with the baseline model (ELM\_Baseline) and the experiments with updated models (See Table 2 for the configuration for each experiment). Gray line represents the ensemble mean of simulations within the good performance zone (as shown in Figure 7) with error bars as the standard deviation and the shaded area indicating the minimum-to-maximum bound. Red open circles are observed monthly averages with the number of daily observations less than 10 days, which are not used for the computation in Figure 7. Optimal – the best simulation for each site; Generic – the simulation with a common decomposition scheme that provides best overall performance for all the sites and will be applied to regional simulation.

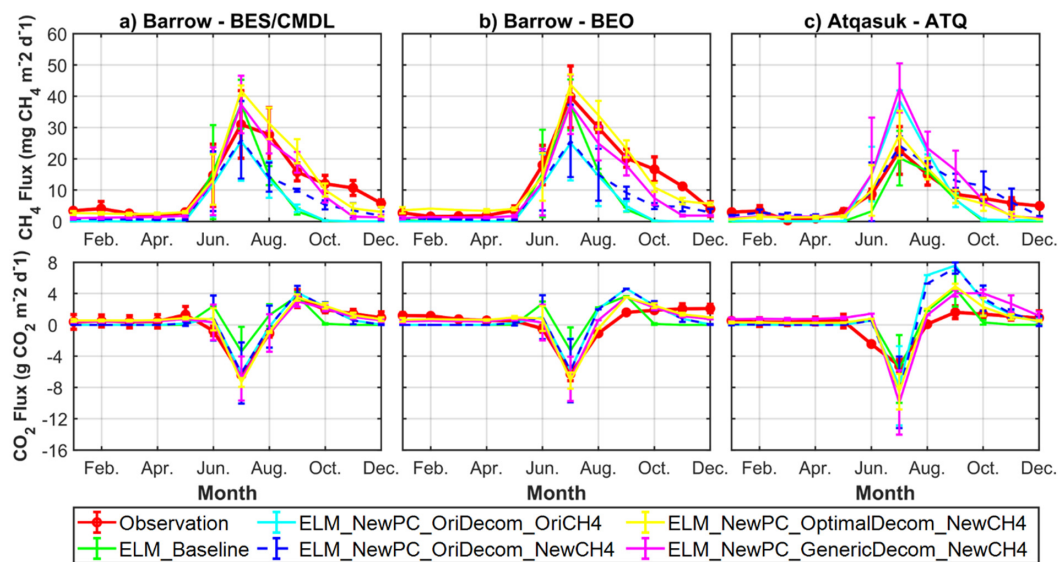


Figure 9: Comparison of multi-year (2013-2017) averaged monthly mean CH<sub>4</sub> (top) and CO<sub>2</sub> (bottom) net flux from simulations and measurements at BES&CMDL, BEO, and ATQ. The error bars represent standard deviation of monthly mean.



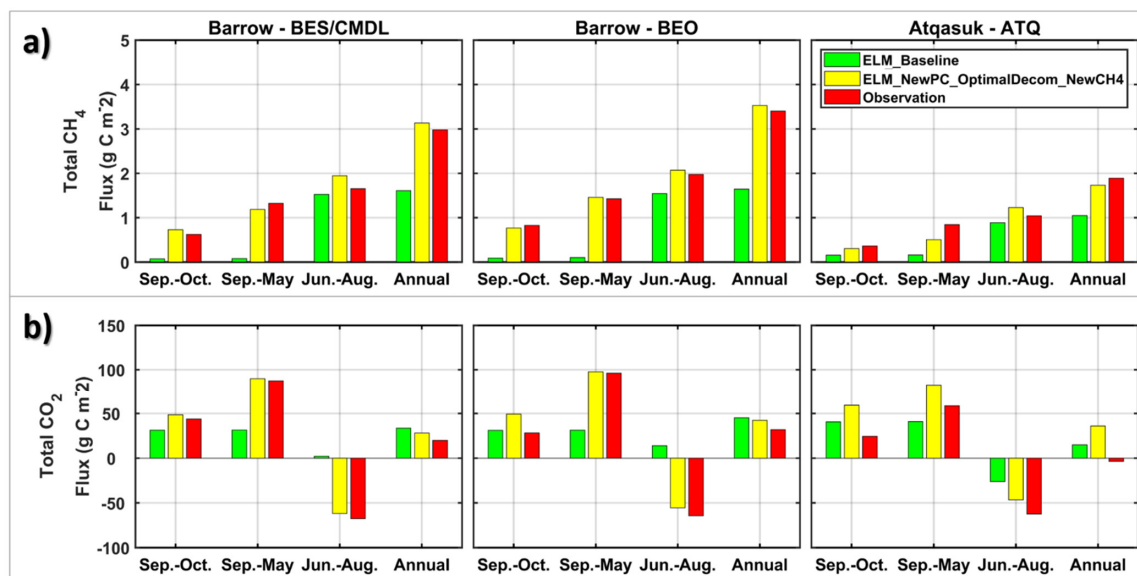


Figure 10: Multi-year (2013-2017) averaged total CH<sub>4</sub> emissions (upper) and CO<sub>2</sub> net fluxes (bottom) during the early cold season (Sep. and Oct.), cold-season period (Sep. to May), warm-season period (Jun. to Aug.), and the annual cycle (Sep. to Aug.) at three of our study sites. Due to the large discontinuity in CO<sub>2</sub> observations, especially over the warm season (shown in Figure 8), the observed annual CO<sub>2</sub> budget is highly uncertain. Still, the cold-season contributions of both CH<sub>4</sub> and CO<sub>2</sub> emissions are greatly improved by the updated ELMV1-ECA (i.e., ELM\_NewPC\_OptimalDecom\_NewCH<sub>4</sub>).